Sensors & Diagnostics

ROYAL SOCIETY OF CHEMISTRY

PAPER

View Article Online
View Journal | View Issue

Check for updates

Cite this: *Sens. Diagn.*, 2023, **2**, 361

Recent advances in MoS_2-based nanomaterial sensors for room-temperature gas detection: a review

Xu Tian,[a] Shanli Wang,[a] Haoyu Li,[a] Mengyao Li,[a] Ting Chen,*[b]
Xuechun Xiao*[a] and Yude Wang *[c]

Received 17th November 2022,
Accepted 22nd December 2022

DOI: 10.1039/d2sd00208f

rsc.li/sensors

The two-dimensional (2D) material, MoS_2, has attracted great attention in the development of room-temperature gas sensors in recent years due to its large specific surface area, ultra-high carrier mobility, strong surface activity, and high adsorption coefficient. However, pristine MoS_2 gas sensors still exhibit some drawbacks such as low sensing response, sluggish recovery process, and incomplete recovery, which are unfavorable for the application of gas sensors. Therefore, significant efforts have been devoted to the design of specific MoS_2-based gas sensors with enhanced sensing properties. In this review, we aim to discuss the recent advances in MoS_2-based nanomaterial sensors for room-temperature gas detection. Firstly, some strategies to improve the gas sensing performance of MoS_2-based gas sensors are introduced, including designing morphologies, creating sulfur vacancies, decorating noble metals, doping elements, introducing light, and constructing composites. Secondly, the types of gases that can be detected by MoS_2-based gas sensors are proposed and summarized, and their sensing mechanisms are also analyzed. Finally, an outlook is presented and the future research directions and challenges are discussed.

1. Introduction

The detection of toxic and harmful gases is important to ensure the safety of life and protect the environment. In the past few decades, semiconductor metal oxide (SMO) gas sensors have been the dominant tools for the detection of toxic gases such as volatile organic compounds (xylene, toluene, formaldehyde (HCHO), ammonia (NH_3), acetone, ethanol, methanol, and isopropanol), flammable and explosive gases (methane (CH_4), hydrogen (H_2), propane (C_3H_8), carbon monoxide (CO), hydrogen sulfide (H_2S)), nitrogen oxides (nitrogen monoxide (NO), nitrogen dioxide (NO_2)), sulfur oxides (sulfur dioxide (SO_2)), and carbon oxides (carbon dioxide (CO_2)). To date, SMO gas sensors still occupy the central position in the field of gas detection due to their high sensing response, fast response/recovery time and excellent reproducibility. However, some deficiencies presented by SMO gas sensors include their poor selectivity and high operating temperature, which have not been addressed to date. In particular, their high operating temperature will be detrimental to energy saving and limit their application in some special fields. Therefore, it is necessary to develop low-power, high-sensing performance gas sensors.

Recently, several reports have revealed that the emerging two-dimensional (2D) materials exhibit a sensing response to toxic gases at low/room temperature, which not only solves the problem of high power consumption of traditional gas sensors to a certain extent but also enable them to be applied in flexible wearable electronic devices to provide great convenience and achieve intelligent life. The 2D materials include reduced graphene oxide (rGO),[1] transition metal dichalcogenides (TMDs),[2] black phosphorus (BP),[3] hexagonal boron nitride (h-BN),[4] and transition metal carbides, nitrides and/or carbonitrides (MXenes),[5] which can be considered as promising gas sensing materials owing to their unique single-atom layer structure. Specifically, they exhibit high specific surface area close to the theoretical extreme, excellent semiconductor performance, unique surface configurations with dangling bonds on their edge sites, and flexible basal planes.[6–10] Among them, the layered TMDs with the composition of MX_2 (M = Ti, Zr, Hf, V, Nb, Ta, Mo, W, Tc, Re, Pd, and Pt and X = S, Se, and Te)[11] have gained intensive attention as gas sensing materials because of their strong

---

[a] *National Center for International Research on Photoelectric and Energy Materials, School of Materials and Energy, Yunnan University, 650091 Kunming, People's Republic of China. E-mail: xchxiao@ynu.edu.cn; Fax: +86 871 65153832; Tel: +86 871 65035570*

[b] *Institute of Materials Science & Devices, School of Materials Science and Engineering, Suzhou University of Science and Technology, Suzhou, 215009, People's Republic of China. E-mail: chenting@mail.usts.edu.cn*

[c] *Key Lab of Quantum Information of Yunnan Province, Yunnan University, 650091 Kunming, People's Republic of China. E-mail: ydwang@ynu.edu.cn*

spin–orbit coupling interaction, tunable electronic properties, and high interaction ability for the adsorption of gas molecules.[12,13] Among the TMDs, the semiconductor MoS_2 and WS_2 with atomically thin-layered structures, lower bandgap, abundant edge active sites, and excellent electrical and/or chemical properties exhibit good gas sensing abilities at room temperature (RT).[14–16] In particular, MoS_2 has become the most ideal gas sensing material[17,18] owing to its ultra-high carrier mobility, high adsorption coefficient, tunable bandgap (1.2–1.9 eV), and excellent field-effect transistor behavior.[19–22] These parameters have a positive impact on the sensitivity and stability of gas sensors and the designability of novel sensing materials based on MoS_2. MoS_2 presents four crystal structures including 1H, 1T, 2H, and 3R, which are defined by the coordination relationship between the Mo and S atoms and the stacking order between their layers, as shown in Fig. 1. The numbers 1, 2, and 3 represent the number of S–Mo–S layers in each unit cell, while the letters T, H, and R represent triangle, hexagonal, and rhombohedral, respectively. The 1T-MoS_2 phase shows metallic nature, whereas the 2H-MoS_2 phase exhibits semiconductor characteristic (n-type). In terms of thermodynamics, besides the 2H phase, three other crystal phases of MoS_2 possess a metastable structure, which can also be transformed under certain conditions.[23] Therefore, the thermodynamically stable 2H-MoS_2 structure dominates current applications.[24]

Recently, several review papers highlighted 2D layered material-based resistive sensors.[8,25,26] These works emphatically discussed the synthesis methods, gas sensing application of TMDs, and the sensing mechanisms of TMDs van der Waals nanocomposite junctions. Considering the advantages of MoS_2 and its potential application in developing room-temperature gas sensors, herein, we mainly review the recent advances of MoS_2 nanomaterial-based gas sensors for room temperature detection. Based on the existing review papers, we further present the development of MoS_2 gas sensors and discuss them in detail. Initially, we discuss some strategies for improving the gas sensing properties of MoS_2. Subsequently, we summarize the types of toxic gases that MoS_2 can sense at RT. Moreover, the sensing mechanisms of MoS_2-based gas sensors towards different gases are also discussed. Furthermore, we conclude this review with some perspectives and outlooks on this new trend in the field of gas sensing.

2. Strategies to improve the gas sensing performance of MoS_2

Although MoS_2 has shown great advantages in the development of room temperature gas sensors, it still faces some challenges, for instance, due to the stacking of the S–Mo–S layers, bulk MoS_2 does not have sufficient contact with gas molecules and forms poor conductive network signals, which lead to a low response value and slow response recovery rate. Especially, the incomplete recovery at RT is a severe challenge for MoS_2-based gas sensors. In this regard, more efforts have been devoted to designing specific MoS_2-based RT gas sensors with enhanced sensing properties. The improvement strategies include designing morphologies, creating sulfur vacancies, decorating noble metals, doping elements, introducing light, and constructing composites. In this part, we summarize the above-mentioned strategies for improving the gas sensing performance of MoS_2 materials.

2.1 Morphology design

For sensing applications, the morphology of MoS_2 plays a crucial role in enhancing the sensing performance by providing more reactive sites. A change in the morphology of

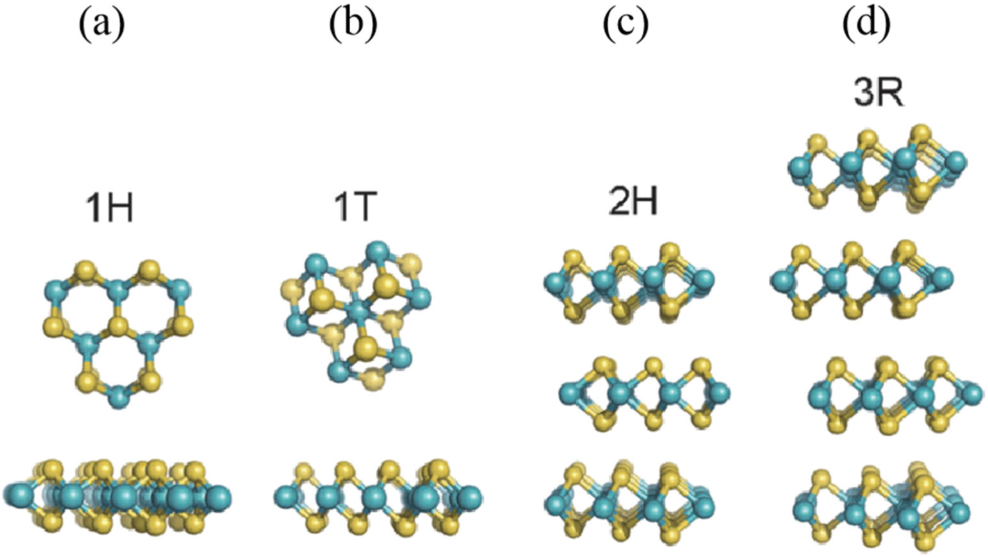

Fig. 1 Different polymorphs or phases of MoS_2: (a) 1H phase, (b) 1T phase, (c) 2H phase, and (d) 3R phase. Reprinted with permission from ref. 24. Copyright 2015, The Royal Society of Chemistry.

MoS_2 refers to its dimensions, which can be varied from zero, one, and two to three-dimensional nanostructures. MoS_2 with different dimensions exhibit unique physical and optoelectronic properties, defects, exposed facets, porosity, atomic configuration,[27] and thus its gas sensing properties will also be different. When MoS_2 is compressed to zero-dimensional, completely special electronic and photophysical properties are generated due to the quantum confinement and edge effects,[28] such as a higher direct bandgap of 3.96 eV,[25] larger edge-to-volume ratio, and higher in-plane electron transport rate. Niu *et al.*[29] synthesized MoS_2 quantum dots (MQDs) *via* the combined high speed shear, sonication and solvothermal treatment of bulk MoS_2 in *N*,*N*-dimethylformamide. Fig. 2a shows the HRTEM image of MQDs with an average size of 7.8 nm. NH_3 and NO_2 gases were recognized by the MQD sensor at RT. The dynamic sensing response of the MQD sensor towards various concentrations of NO_2 (Fig. 2b) and NH_3 (Fig. 2c) revealed that it had almost the same response value for both gases. However, the recovery was not complete due

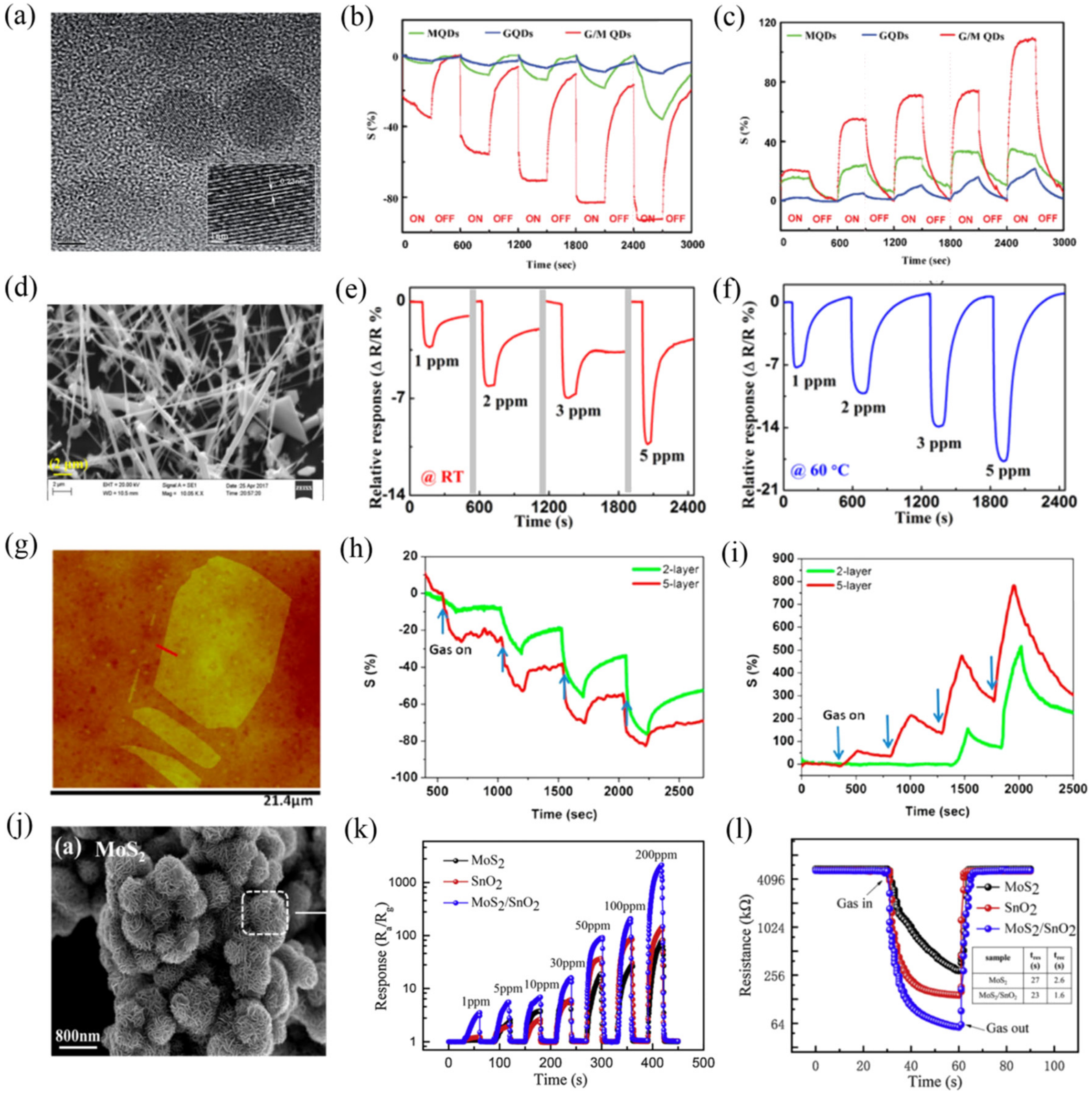

Fig. 2 (a) HRTEM of MQDs. Dynamic response of the MQDs (green) upon exposure to increasing (b) NO_2 and (c) NH_3 concentrations. Reprinted with permission from ref. 29. Copyright 2016, The Royal Society of Chemistry. (d) SEM image of MoS_2 nanowires. Transient response of the MoS_2 nanowire sensor at (e) room temperature (RT) and (f) 60 °C. Reprinted with permission from ref. 30. Copyright 2018, AIP Publishing. (g) AFM image of single-layer MoS_2 sheet. Comparative two- and five-layer MoS_2 cyclic sensing performances with (h) NH_3 and (i) NO_2 (for 100, 200, 500, and 1000 ppm). Reprinted with permission from ref. 31. Copyright 2013, the American Chemical Society. (j) SEM images of MoS_2 nanoflowers. (k) Responses curves of MoS_2, SnO_2, and SnO_2/MoS_2 sensors to various concentrations (1–200 ppm) of NH_3. (l) Resistance curves of MoS_2, SnO_2, and SnO_2/MoS_2 to 50 ppm of NH_3 at room temperature (the insert table indicates the response and recovery times). Reprinted with permission from ref. 33. Copyright 2020, Elsevier B.V.

to the high-energy binding sites of the MQDs. This research team is working on how to balance the relationship between the selectivity and fast desorption in their further study.

One-dimensional MoS_2 nanostructures include nanowires and nanotubes. Their electronic properties also vary with a change in their diameter and chirality, for example, MoS_2 nanotubes exhibit a larger bond length and smaller semiconducting bandgap than that of the bulk MoS_2 nanosheets.[25] Kumar *et al.*[30] reported the fabrication of an NO_2 sensor based on one-dimensional MoS_2 nanowires (Fig. 2d), which were synthesized using chemical transport reaction through controlled turbulent vapor flow. The results showed that the MoS_2 nanowire sensor displayed a high sensing response to NO_2 gas; however, it still faced the problem of incomplete recovery at RT due to the strong binding between NO_2 and the reactive sites of MoS_2, as shown in Fig. 2e. Thus, to address its difficult recovery and low response at RT, this team investigated its sensing behavior at a high operating temperature (60 °C) (Fig. 2f). They proposed that the relatively quick adsorption and desorption of NO_2 gas molecules from MoS_2 at 60 °C were attributed to its high conductivity and the rapid interaction of gas molecules with the exposed edge sites of the nanowires. Also, they indicated that the oxygen and humidity occupy a large number of reactive sites in the MoS_2 nanowires at RT, and thus there were less NO_2 molecules to participate in the reaction, resulting in a weak response to NO_2 at RT.

MoS_2 with monolayer or few-layer two-dimensional nanostructures is currently the most studied in the field of gas sensing. Monolayer MoS_2 shows a direct bandgap of 1.8 eV, while bulk MoS_2 possesses an indirect bandgap of 1.2 eV. This transition endows monolayer MoS_2 with superior semiconductor properties. Meanwhile, monolayer or few-layer MoS_2 expose abundant edge sites and a high specific surface area, which may be beneficial for the absorption of gas molecules. In addition, it also exhibits high toughness and has potential to be applied on flexible substrates. Late *et al.*[31] investigated whether the single-layer MoS_2 is an ideal structure for enhancing the gas sensing performances. The AFM image of single-layer MoS_2 is shown in Fig. 2g. They found that the single-layer MoS_2 device was not stable over time. For clarity and brevity, they examined the gas sensing responses of two-layer and five-layer MoS_2 to various concentrations of NH_3 (Fig. 2h) and NO_2 (Fig. 2i) gases at RT because they were the thinnest and the thickest, respectively. The results showed that five-layer MoS_2 had better sensitivity compared to that of the two-layer MoS_2, they agreed that this may be due to the different electronic structures with a variation in thickness (layering). However, this issue is complicated and needs further study. Li *et al.*[32] prepared few-layer MoS_2 nanosheets *via* mechanical exfoliation for the RT detection of NO_2. This sensor achieved high responsivity and ultrafast recovery behavior to NO_2. They proposed that the high sensitivity was caused by the thin thickness of MoS_2, while the fast recovery time was attributed to the weak van der Waals force between NO_2 and MoS_2.

Three-dimensional nanoflower-like MoS_2 (Fig. 2j) assembled by several nanosheets has also received great attention for gas sensing. MoS_2 nanoflower is mainly synthesized *via* a hydrothermal process. Wang *et al.*[33] prepared MoS_2 nanoflowers *via* a simple hydrothermal method at 200 °C for 22 h. Fig. 2k shows the dynamic sensing response curves of MoS_2, SnO_2, and SnO_2/MoS_2 sensors towards different concentrations of NH_3 at RT. It was observed that the nanoflower-structured MoS_2 and its nanocomposite-based gas sensors exhibited high sensing response values. The resistance curves (Fig. 2l) of the MoS_2, SnO_2, and SnO_2/MoS_2 sensors exposed to 50 ppm NH_3 revealed that they displayed a very fast response and recovery rate (27/2.6 s for MoS_2 sensor), which seems to be very interesting. Thang *et al.*[34] discussed the effect of the hydrothermal growth times of 24, 36, 48, and 60 h on the sensitivity of the obtained MoS_2 nanoflowers and concluded that 48 h was the best growth time. The 48 h-MoS_2 nanoflowers showed a high gas response of 67.4% and high selectivity to 10 ppm NO_2 at RT. The superior sensing performance of the 48 h-MoS_2 nanoflower was ascribed to its largest specific surface area, smallest crystallite size, and lowest activation energy among the prepared samples. The dynamic resistance characteristic revealed that the 48 h-MoS_2 sensor exhibited complete response and recovery to NO_2 gas at RT. The authors ascribed this result to the high specific surface area and defects of the 48 h-MoS_2. They proposed that several factors such as high specific surface area, defective/strained surface, and weak van der Waals binding between the target gas and the MoS_2 surface affected the gas adsorption and desorption behavior. However, the complete recovery mechanism of the MoS_2 sensor is a complex case, and there are some disputes due to the combined effects of physi- and chemi-sorption, role of defects sites and transduction mechanism.[35]

2.2 Vacancy promotion

The lack of adsorption sites in MoS_2 has become the main bottleneck in realizing a high sensing performance at RT. It has been theoretically and experimentally proven that the vacancies in MoS_2 act as high-energy binding sites and play an important role in enhancement the gas sensing performance. The vacancies mainly refer to two types, *i.e.*, Mo vacancy and S vacancies. However, the lower binding energy of S vacancy (2.12 eV) compared to Mo vacancy (6.20 eV) makes its construction more desirable, wherein the S vacancy is defined as the absence of one or two sulfur atoms per MoS_2.[36,37] The strategy of generating S vacancies in MoS_2 aims to reduce the Gibbs free energy of gas adsorption,[38] increase the amount of charge transfer,[39] facilitate molecular adsorption and chemical functionalization,[40] offer abundant active sites, and even cause the dissociation of gas molecules.[41] At present, S vacancies can be achieved by microwave-hydrothermal treatment, liquid-phase ultrasonic exfoliation, metal quantum dot loading,[42] electron irradiation and thermal annealing.[36,43,44]

Xia *et al.*[43] discussed the NO_2 gas sensing performance of conventional MoS_2 (C-MoS_2) and sulfur-vacancy-enriched MoS_2 (SV-MoS_2) under dark and near-infrared (NIR) light conditions at RT, respectively. The researchers employed X-ray diffraction (XRD), electron paramagnetic resonance (EPR), and X-ray photoelectron spectroscopy (XPS) characterization techniques to prove the presence of sulfur vacancies, enriched S vacancy defects, and defect-related surface species in the MoS_2 samples, as shown in Fig. 3a–c, respectively. The response in Fig. 3d reveals that the SV-MoS_2 sensor showed a better gas sensing performance to 200 ppm NO_2 than the C-MoS_2 sensor in both the dark and under NIR illumination, which can be ascribed to the presence of more active centers and increased electron transfer introduced by the S vacancies. Moreover, the response value of the SV-MoS_2 sensor under NIR light had a significant improvement compared to that in a dark environment, while a slight increase occurred in the C-MoS_2 sensor, demonstrating that the S vacancy-induced photocurrent could effectively detect NO_2 gas at RT.

Zhang *et al.*[45] introduced S vacancies in 2D-in-3D architecture MoS_2 by high temperature annealing in an argon atmosphere. They compared the sensing properties of different MoS_2 samples obtained at various annealing temperatures of 0 °C, 550 °C, 700 °C, and 850 °C to NO_2 at RT. The results showed that the hierarchical MoS_2 annealed at 850 °C exhibited an extremely high gas sensing performance in terms of sensitivity (Fig. 3e), selectivity and stability. These excellent sensing properties can be attributed to the large number of S vacancies in MoS_2, which were generated upon high temperature annealing and led to the strong interlayer coupling and spin–orbit coupling effects. The generation of S vacancies was confirmed by the decrease in the S : Mo ratio (Fig. 3f) under high temperature annealing by XPS measurements. In this regard, S vacancies play an extremely important role in improving the gas sensing performance of MoS_2 materials.

In addition, density functional theory (DFT) calculations also revealed that MoS_2 rich in S vacancies possessed a higher sensing performance to gases. Li *et al.*[46] calculated the adsorption properties and charge transfer of NO molecules on monolayer MoS_2 (MoS_2-MLs), S vacancy-defective MoS_2-MLs (S-vacancy), and vacancy complex of Mo and its nearby three sulfur vacancies (MoS3-vacancy) by density functional theory (DFT). The adsorption energy of an NO molecule on the most stable adsorption models of MoS_2-MLs, S-vacancy, and MoS_3-vacancy was 0.14 eV, 2.57 eV and 1.95 eV, respectively. The theoretical results demonstrated that the MoS3-vacancy and S-vacancy-defective MoS_2-MLs showed stronger chemisorption and greater electron transfer effects than pure MoS_2-ML,

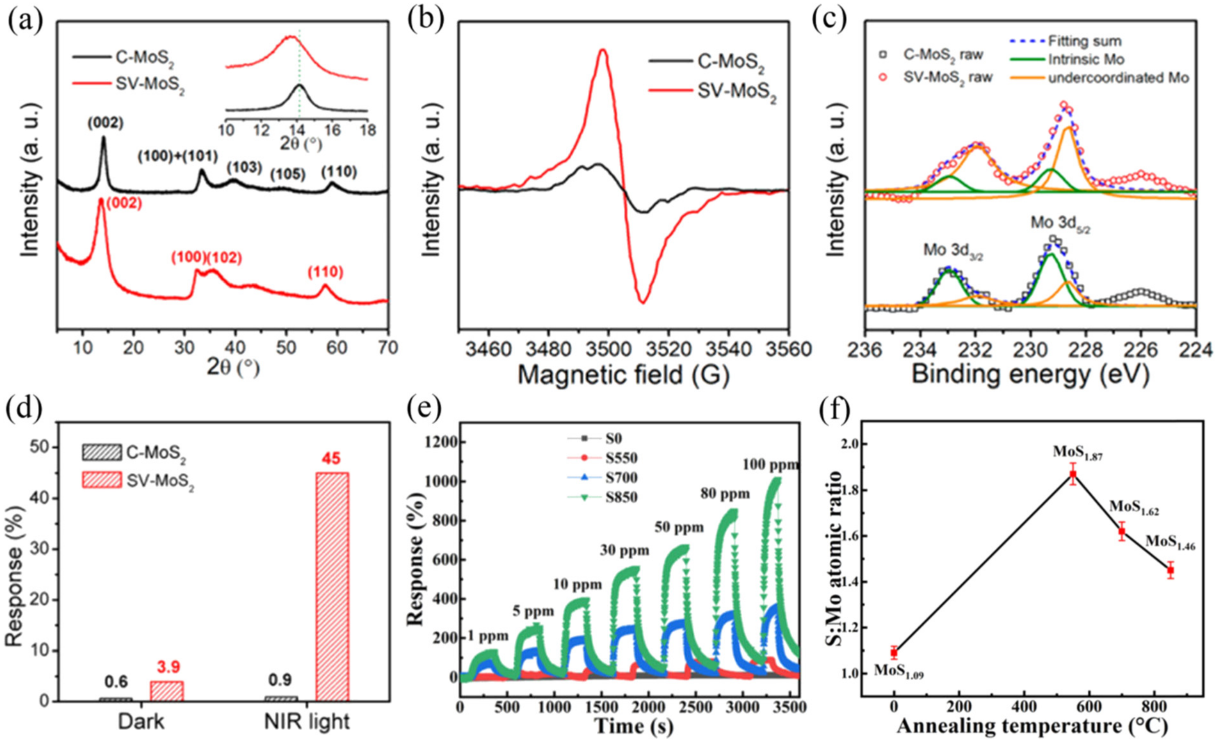

Fig. 3 (a) XRD, (b) EPR, (c) Mo 3d XPS spectra of C-MoS_2 and SV-MoS_2 samples. (d) Gas responses of C-MoS_2 and SV-MoS_2 sensors in the dark and under NIR illumination. Reprinted with permission from ref. 43. Copyright 2019, the American Chemical Society. (e) Dynamic response curves of the S0, S550, S700, and S850 sensors toward different concentrations of NO_2 at room temperature. (f) Corresponding S : Mo atomic ratio of S0, S550, S700, and S850. Reprinted with permission from ref. 45. Copyright 2022, Elsevier B.V.

implying that S-vacancy defects can effectively improve the NO sensing performance of MoS_2.

Although the vacancies on the surface of MoS_2 acts as active sites for the adsorption of gas molecules, their high adsorption energy will also result in a slow response and recovery rate.[35]

2.3 Noble metal decoration

The decoration of noble metals (NMs) on MoS_2 has also been reported as another effective strategy to improve its gas sensing properties. NMs such as Au, Ag, Pt, Pd, Rh, and Ru are usually used as effective catalysts to enhance the surface reactivity of sensing materials and accelerate the reaction between the adsorbed oxygen species and the gas molecules.[47] Meanwhile, they can also change the electron accumulation and enhance the electron transfer due to the different work functions between the NMs and sensing materials. Moreover, NMs possess affinity for some specific gas molecules and assist in overcoming the problem of selectivity to a certain extent.[48]

Jaiswal *et al.*[49] reported the preparation of a vertically aligned edge-oriented MoS_2 hybrid nanostructured thin film decorated with Pd nanoparticles (Pd/MoS_2) on quartz and Si substrates using the DC magnetron sputtering technique. The 2D and 3D AFM micrographs of the Pd-functionalized vertically aligned MoS_2 thin film are shown in Fig. 4a and b, respectively. The Pd/MoS_2 hybrid film sensor exhibited an enhanced response of 33.7% and fast response/recovery rate (~16/38 s) compared to the pristine MoS_2 thin film sensor (1.2% response value and ~29/158 s response/recovery time) to 500 ppm H_2 gas at RT (Fig. 4c). The enhancement in the H_2 gas sensing performance of the Pd/MoS_2 hybrid film sensor can be attributed to three aspects. Firstly, the catalytic activity of the small Pd nanoparticles endowed the hydrogen molecules with efficient decomposition ability. Secondly, the unique porous nanostructure of the vertically aligned edge-enriched MoS_2 possessed a higher specific surface area. Finally, the Schottky barrier at the junction between Pd and MoS_2 increased the electrical resistance in air due to the barrier height, becoming more sensitive to a change in H_2 resistance.

Halvaee *et al.*[50] synthesized Ag/MoS_2 nanorods *via* the hydrothermal method. This sensor displayed a selective sensing response for methanol vapor at RT. Firstly, the researchers discussed the effect of different amounts of Ag nanoparticles on the response of the sensor. They found that the mass ratio of 2 wt% Ag nanoparticles loaded on MoS_2 resulted in the best methanol sensing response. The improved gas sensing properties can be ascribed to the catalytic oxidation and chemical sensitization of Ag nanoparticles. Meanwhile, the selectivity of Ag/MoS_2 to methanol was much better than that of pure MoS_2. In addition to the small size of methanol, which could easily penetrate the layered MoS_2, Ag had a better decoration effect to improve the selectivity.

Park *et al.*[51] prepared two-dimensional MoS_2 *via* a metal organic chemical vapour deposition (MOCVD) method, and

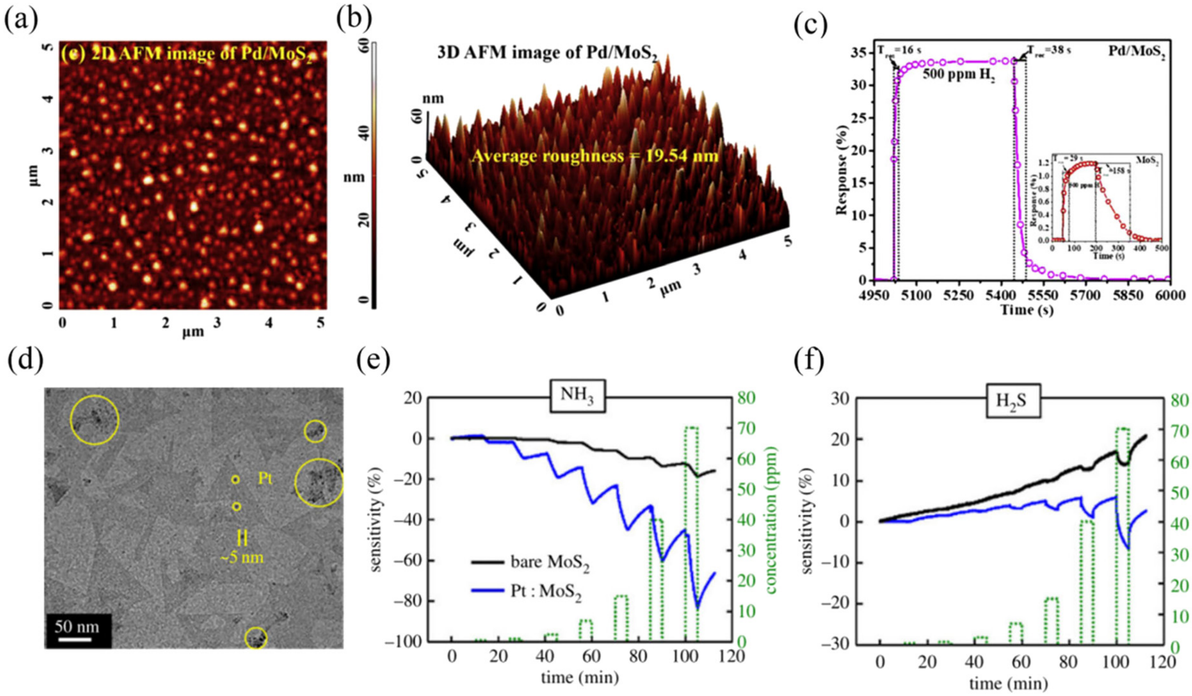

Fig. 4 (a) 2D and (b) 3D AFM micrographs of Pd-functionalized vertically aligned MoS_2 thin film. (c) Sensor response curve of the Pd/MoS_2 hybrid and pristine MoS_2. Reprinted with permission from ref. 49. Copyright 2020, Elsevier B.V. (d) TEM images of the Pt/MoS_2. Gas-sensing characteristics of the MoS_2 and Pt/MoS_2 gas sensors for (e) NH_3 and (f) H_2S. Reprinted with permission from ref. 51. Copyright 2020, IEEE Xplore.

subsequently modified its surface with Pt particles (Fig. 4d). Pt particles have a double p-type doping effect compared to Au particles and possess good corrosion and oxidation resistance. Accordingly, this sensor recognized both NH_3 and H_2S gases at RT; however, the response for H_2S was lower than that for NH_3, as shown in Fig. 4e and f, respectively, confirming that there was less charge transfer between H_2S and Pt/MoS_2. Meanwhile, the response value of Pt/MoS_2 for the target gases was higher than that of bare MoS_2, demonstrating that the Pt particles made an excellent contribution to the improvement in gas sensing performance.

2.4 Element doping

Element doping refers to a change in lattice constant due to the incorporation of dopants in the lattice of MoS_2 or replacement of the Mo, S lattice sites. In this process, the binding energy will be greatly enhanced and defects will be formed to become new active sites, and the electrical properties will also be changed due to the decrease in the electron–hole recombination rate.[52] The doped elements can be divided into metal and nonmetal, where the metal dopants include Zn, W, Nb, Fe, Co, Ni, Cu, Ti, V, Ta, Al, and Ga,[45,53–58] and nonmetal dopants include N, Si, B, N, P, and Cl.[59–61] However, most doping strategies focus on theoretical calculations based on density functional theory (DFT),[62–65] where theoretical results reveal that doped-MoS_2 sensors exhibit a higher adsorption energy, stronger noncovalent interaction, greater carrier transport number, and faster conductivity rate to target gases.[60,62,63] Therefore, more efforts should be devoted to the experimental exploration of doping MoS_2. At present, some experimental studies have been reported.

Wu *et al.*[59] designed an N element-doped MoS_2 gas sensor by controlling the solvothermal temperature to realize the conversion of MoS_2 from n-type to p-type. The researchers proposed that doping could also address the challenge of sluggish sensing of MoS_2 at RT owing to the adjustable active sites and electrical property. Fig. 5a displays the gas sensing response value of pristine MoS_2 and optimal N-doped MoS_2 ($NMoS_2$-2) sensors to various concentrations of NO_2 at RT. It was observed that the $NMoS_2$-2 sensor showed obvious p-type semiconductor feature because the N atoms have one less valance electron than the S atoms in the MoS_2 matrix. Meanwhile, the sensing response value of the $NMoS_2$–2 sensor was not obviously improved compared to that of the pristine MoS_2. However, the fast response/recovery rate (Fig. 5b and c) of the $NMoS_2$-2 sensor revealed that there was a superior fast charge transfer character, as confirmed by the

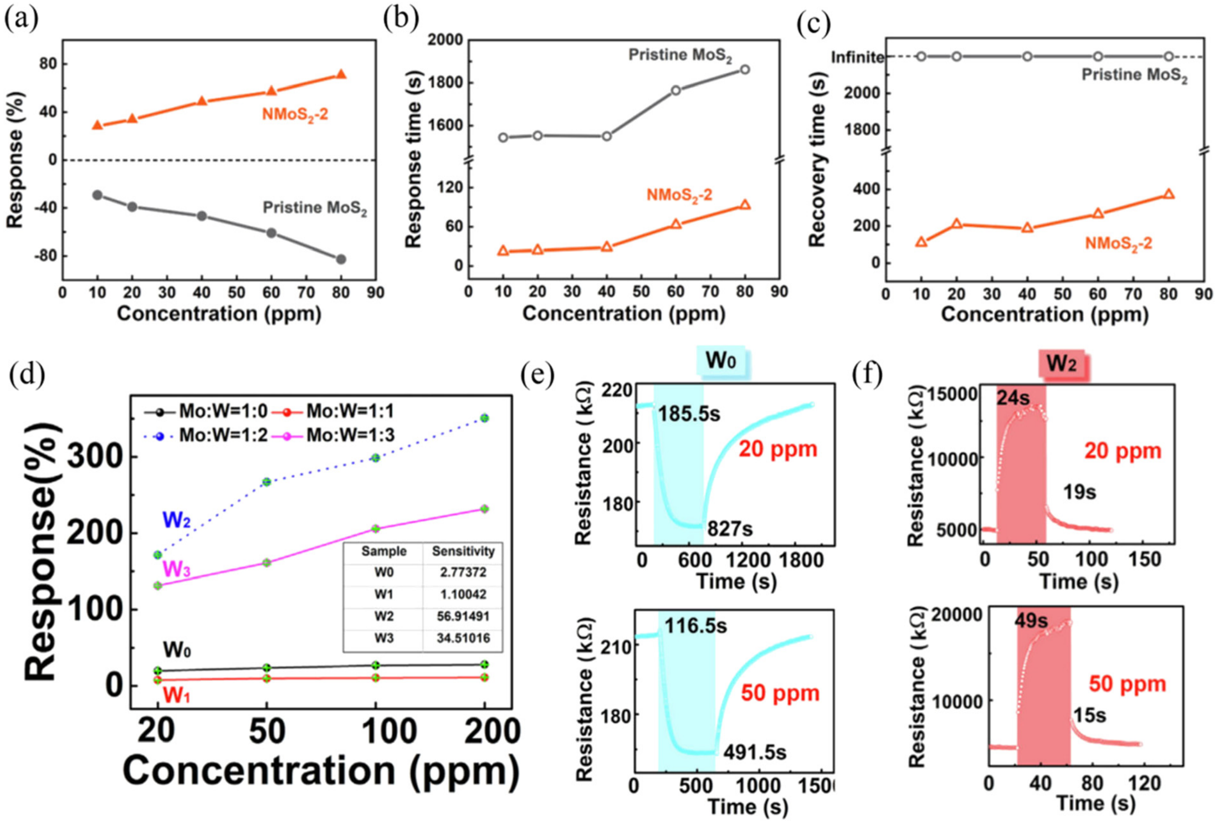

Fig. 5 (a) Response, (b) response time, and (c) recovery time of $NMoS_2$-2 and pristine MoS_2 upon exposure to 10, 20, 40, 60, and 80 ppm NO_2. Reprinted with permission from ref. 59. Copyright 2021, Elsevier B.V. (d) Response value *versus* NO_2 concentration for W_0–W_3. (e) Transient response characteristic of (e) W_0 and (f) W_3 at 20 and 50 ppm NO_2. Reprinted with permission from ref. 53. Copyright 2020, Elsevier B.V.

Hall effect. DFT calculations revealed that there was a favorable surface interaction between the N-doped MoS_2 and NO_2 molecules after N doping. Therefore, N-doping in MoS_2 resulted in a significant improvement in NO_2 sensing response/recovery ability.

Liu *et al.*[53] synthesized W-doped MoS_2 sensors with different W ratios *via* a hydrothermal method. The results showed that appropriate ratios between Mo and W were conducive to enhancing the NO_2 sensing properties at RT. As shown in Fig. 5d, when the Mo : W ratio was 1 : 2 (named W_2), the sensing response was observed to be the best for various concentrations of NO_2. Furthermore, the response/recovery times of the W-doped MoS_2 (W_2) sensor (Fig. 5f) was greatly improved compared to the undoped MoS_2 sensor (Fig. 5e), which was mainly attributed to the effective suppression of defects by W doping.

Briefly, according to the current research results, the doping method can be regarded as an effective method to solve the slow response/recovery ability of MoS_2.

2.5 Light assistance

Light assistance has shown promise for the activation of gas sensor materials. MoS_2 possesses a tunable band gap and excellent photoelectrical properties, and thus it is also an effective way to improve its gas sensing performance by light activation. Light activation mainly assists the recovery rate of MoS_2 gas sensors,[66] and the photochemical reaction occurring between the light-generated electron/hole carriers in MoS_2 and adsorbed gas molecules promotes the desorption process.[67,68] At present, two light activation gas sensing mechanisms have been proposed, *i.e.*, the "optoelectronic" and "photocatalytic" mechanisms. The optoelectronic mechanism refers to the generation of a photocurrent, which regulates the conductivity of the material and causes a large change in the resistance of the sensor upon gas exposure.[15,69] The photocatalytic mechanism considers the process of photocatalytic oxidation of reducing gases into NO_x, CO_2 and H_2O,[70,71] thus accelerating the chemisorption reaction between the sensing material and target gases.

Wang *et al.*[72] proposed the visible-light photocatalytic enhancement gas sensing mechanism based on MoS_2/rGO hybrids for the detection of formaldehyde (HCHO) at RT. The comparison of response/recovery times of the MoS_2/rGO sensor to 10 ppm HCHO in the dark and under visible-light illumination, as shown in Fig. 6a, which revealed that the visible light accelerated the gas molecule adsorption/desorption process. In addition, the O_2-TPD spectra of MoS_2, as shown in Fig. 6b, demonstrated that visible light induced the adsorption of more oxygen species. Meanwhile, CO_2 peaks at 1358 and 1572 cm^{-1} and broad H_2O peak at around 3420 cm^{-1} were observed by *in situ* IR spectroscopy (Fig. 6c) when MoS_2 was exposed to HCHO and illuminated by visible

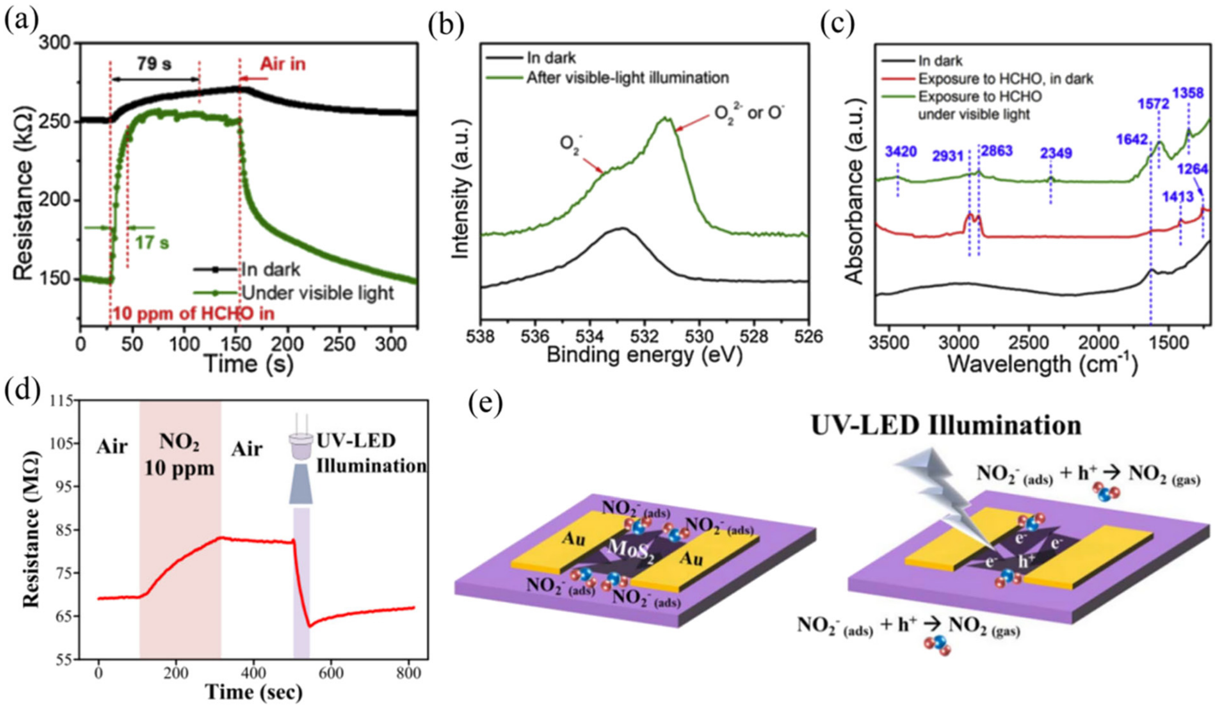

Fig. 6 (a) Dynamic resistance variations of the MoS_2/rGO sensor to 10 ppm HCHO in the dark and under visible-light illumination. (b) O 1s XPS spectra of MoS_2 in the dark and after visible-light illumination for 5 min. (c) *in situ* IR spectra of the MoS_2 sample under different conditions. Reprinted with permission from ref. 72. Copyright 2020 Elsevier B.V. (d) Transient sensor response upon exposure to 10 ppm NO_2, and a UV-LED was turned on during the recovery process. (e) Schematic of the recovery mechanism for MoS_2 under UV-LED illumination after NO_2 exposure. Reprinted with permission from ref. 73. Copyright 2019, IOP Publishing Ltd Printed in the UK.

light, which suggests that the visible-light illumination triggered the photocatalytic oxidation of HCHO to CO_2 and H_2O on the surface of MoS_2.

Kang *et al.*[73] reported that UV light-illuminated MoS_2 could achieve the recovery of its initial resistance when NO_2 gas was withdrawn at RT (Fig. 6d). They believed that excitons were generated in MoS_2 under UV light illumination, which could be separated into electrons and holes when an in-plane electric field of 2 kV cm^{-1} was applied. The absorbed NO_2^- by capturing electrons from MoS_2 previously would react with the photo-generated holes to result in the formation of NO_2, which accelerated the desorption process (Fig. 6e). Meanwhile, the photo-generated electrons remaining in the conduction band of MoS_2 would decrease the resistance. Thus, this explains why UV-light illumination caused a rapid return to the initial resistance of the platform after releasing NO_2 gas.

2.6 Construction of composites

The construction of MoS_2-based composite gas sensors has been demonstrated to be one of the most effective methods to improve the gas sensing properties. In comparison to pure MoS_2, MoS_2 nanocomposites with well-designed architectures are more desirable. The types of composites include binary and ternary structures, which can achieve an enhancement in gas sensing performance by making use of the merits of each component to generate synergistic effects and construct heterojunctions. The heterojunctions include n–n, n–p, and p–p types; however, MoS_2 can exhibit either a p- or n-type gas sensing response to reductive vapor depending on its annealing temperature in air.[74] The heterojunctions can effectively rectify the electron transfer at the contact surface of two materials and increase the interface barrier due to their different Fermi levels, which can significantly improve the gas sensitivity of composite sensing materials. Moreover, MoS_2-based composites accelerate the response/recovery rate of the sensor to some extent. Therefore, constructing composites of MoS_2 may be one of the most effective modification methods. Materials compounded with MoS_2 can be classified into the following categories:

(i) Metal oxide semiconductors: n-type CeO_2,[75] ZnO,[76] SnO_2,[77] WO_3,[78] In_2O_3,[79] TiO_2,[80] and MoO_3 (ref. 81) and p-type CuO,[82] Co_3O_4,[83] NiO,[84] Cu_2O,[85] PANI,[86] and PPy.[87]

Bai *et al.*[88] reported the preparation of a room-temperature NO_2 gas sensor based on an MoS_2/SnO_2 p–n heterojunction. MoS_2 exhibited p-type semiconductor behavior in this work, which was induced by the oxygen vacancies/defects. The MoS_2 nanoflakes were vertically grown on the SnO_2 nanotubes *via* electrospinning, and subsequent hydrothermal method, as shown in the SEM image in Fig. 7a. The optimal MoS_2@SnO_2-2 sensor (the mole ratio of Sn : Mo

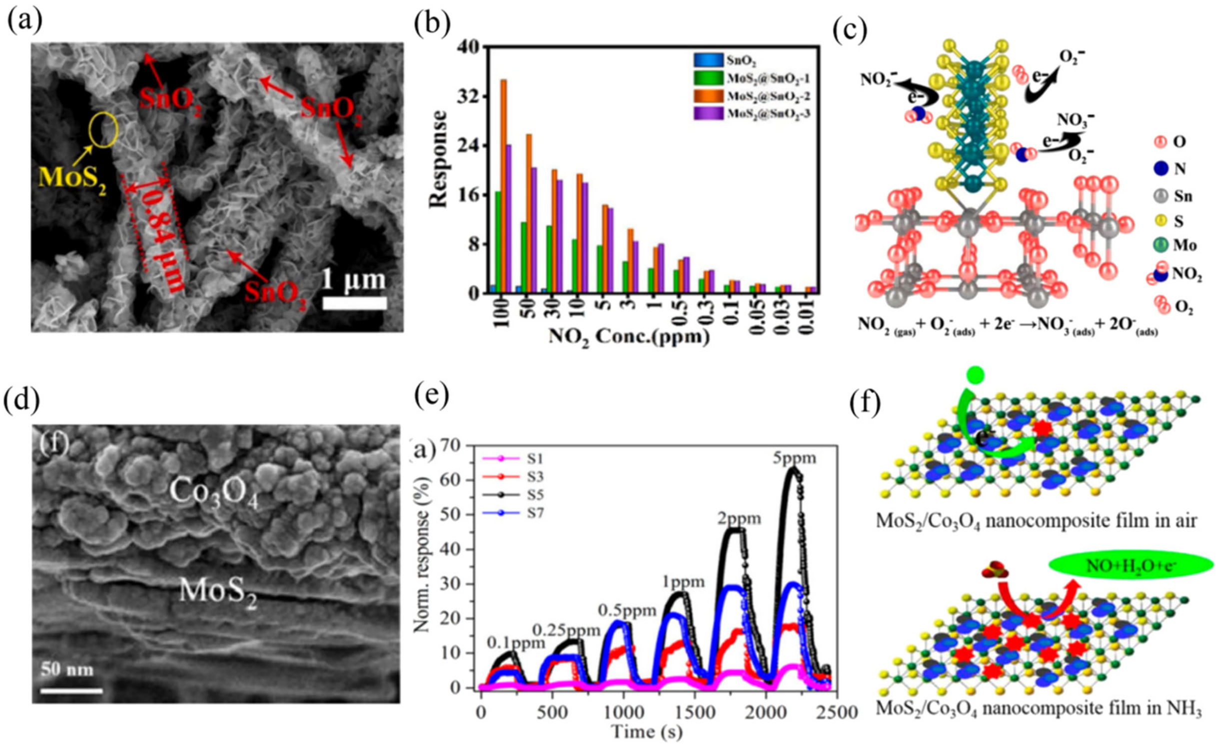

Fig. 7 (a) SEM images of MoS_2@SnO_2-2 nanocomposite. (b) Responses of the prepared sensors to different concentrations of NO_2. (c) Schematic of sensing mechanisms of MoS_2@SnO_2-2 nanocomposite. Reprinted with permission from ref. 88. Copyright 2021 Elsevier B.V. (d) SEM image of Co_3O_2/MoS_2 sample. (e) NH_3 gas-sensing properties of LbL self-assembled MoS_2/Co_3O_4 nanocomposite sensors with different layers. (f) Schematic of the sensing mechanism of n-type MoS_2/p-type Co_3O_4 hybrid in air and ammonia. Reprinted with permission from ref. 89. Copyright 2017, the American Chemical Society.

was 1 : 1/2) exhibited the highest sensing response value compared to the other mole ratio sensors and pristine SnO_2 sensor towards different concentrations of NO_2 gas (Fig. 7b). Meanwhile, its response/recovery times (2.2/10.54 s) were also fast. The enhancement in the gas sensing properties could be attributed to the unique morphological structure, high specific surface area, large number of sulfur edge active sites, and p–n heterojunction created between MoS_2 and SnO_2. The sensing mechanism could be explained by the surface depletion layer model caused by oxygen adsorption, as shown in Fig. 7c. The ionized chemisorbed oxygen (O_2^-) produced on the surface of sensing material formed NO_3^- by introducing NO_2 gas due to the oxidation reaction. This process caused a change in the carrier concentration, and especially after the formation of heterojunctions, this change would be greater.

Zhang *et al.*[89] fabricated a Co_3O_4/MoS_2 p–n heterojunction nanocomposite (Fig. 7d) sensor on interdigital electrodes *via* the layer-by-layer self-assembly route. Firstly, they discussed the effect of the number of layers on the composite assembled with one, three, five, and seven layers (S1, S3, S5, and S7) on the NH_3 gas sensing performance at RT, respectively. The five-layered Co_3O_2/MoS_2 sensor exhibited the best NH_3 sensing response, as shown in Fig. 7e. The sensing mechanism could also be ascribed to the large change in the width of the depletion layer when exposed to an air and NH_3 atmosphere, respectively, which was caused by the p-n heterojunction. NH_3 reacted with the adsorbed O_2^- to produce NO gas and release electrons (Fig. 7f), which resulted in an increase in the resistance of the sensor.

(ii) Two-dimensional materials: transition metal dichalcogenides (TMDs) such as WS_2,[90,91] WSe_2,[92] and VS_2;[93] hexagonal boron nitride (h-BN);[94] transition metal carbides, nitrides and/or carbonitrides such as $Ti_3C_2T_x$ MXene;[95] reduced graphene oxide (rGO);[96–98] and graphene.[99]

The MoS_2 composites with other TMDs can change the amplitude of variation in target gases to increase the response value. For example, Zheng *et al.*[100] synthesized 2D van der Waals junctions by stacking n-type and p-type atomically thin MoS_2 films *via* chemical vapor deposition (CVD) and soft-chemistry route, respectively. This idea was very interesting and meaningful. They employed the two different semiconductor characteristics of MoS_2 to construct a p-n junction sensor. This sensor displayed outstanding sensitivity to NO_2 at RT, which was much higher than that of pristine n-type and p-type MoS_2. The enhanced sensing performance was ascribed to the built-in electric field generated at the p-n interface, which resulted in a huge change in resistance upon contact with NO_2 molecules.

Ikram *et al.*[91] reported the preparation of an MoS_2@WS_2 heterojunction sensor for the effective detection of NO_2 at RT. When the sensor contacted with NO_2 molecules, more electrons in the composite could be captured by NO_2 compared to that of the single MoS_2 or WS_2 component due to the double-electron supply effect, which caused a higher change in resistance. In addition, Zhang *et al.*[93] proposed that the combination of different TMDs with different geometrical and electronically energetic alignments exhibited unique features. Porous VS_2 with intrinsic metallic and highly conductive characteristics was epitaxially grown on MoS_2 nanosheets. They constructed an MoS_2/VS_2 quartz crystal microbalance sensor, which showed high sensitivity and selectivity to NH_3. The metallic VS_2 transferred electrons to MoS_2, causing more electrons to accumulate on the side of MoS_2, which contributed to the O_2 acquiring a large number of electrons to form adsorbed oxygen and increased the initial resistance of the heterostructure in air. Therefore, it showed better sensitivity than the pure MoS_2 and VS_2.

Liu *et al.*[94] designed an MoS_2 gas sensor capped with a thin layer of h-BN. They found that the h-BN layer capped on the MoS_2 layer improved the device stability, robustness and anti-fading capacity, while leaving the gas sensing capability unchanged due to the strong oxidation resistance of h-BN.

In the case of $Ti_3C_2T_x$ MXene, it has high conductivity and active termination groups of T_x = –F, –OH, and –O. Yan *et al.*[101] analyzed the NO_2 sensing reinforcement of the MoS_2/$Ti_3C_2T_x$ MXene composite sensor, where they considered that the excellent electrical property of MXene will make up for the deficiency of MoS_2 in this respect. A large number of carriers was transferred from MXene to MoS_2 to create a similar Fermi energy level. The role of MXene was similar to the above-mentioned metallic VS_2. In addition, the surface active groups would be more conducive to adsorbing the NO_2 oxidizing gas.

Graphene and rGO with a large surface area and high charge carrier mobility, which have been considered as alternative sensing material candidates or gas sensing performance modification materials. Graphene can be used to detect individual molecules, causing the ultimate sensitivity.[102] Sangeetha *et al.*[103] reported that the enhanced gas sensing properties of an MoS_2/graphene sensor towards NO_2 including outstanding sensitivity and rapid response/recovery times (22/35 s) were attributed to the synergistic effect of the two materials. The MoS_2 nanoparticles connected with graphene promoted the absorption of more gas molecules in the presence of evanescent wave light. Compared with graphene, rGO is rich in surface vacancies and oxygen functional groups.[104,105] Chen *et al.*[96] constructed 3D MoS_2/rGO composites *via* a low temperature self-assembly method as a low-temperature NO_2 gas sensor. They believed that the improvement in the gas sensing performance of MoS_2/rGO compared to pure MoS_2 and rGO in addition to the contribution of heterojunction between the rGO nanosheet and MoS_2 nanoflowers, was attributed to the chemically active sites, large surface area, and van der Waals forces of rGO, which are also advantageous for gas adsorption.

(iii) Other functional materials: multi-walled carbon nanotubes (MWCNT),[106] poly(3-hexylthiophene) (P3HT),[107] C_3N_4,[108] PbS,[109] GaN,[110] CdTe,[111] ZnS,[112] SnS_2,[113] *etc.*

MoS_2 composites with other functional materials also combine the merits of these materials such as high electrical conductivity, unique electronic transfer channels, similar sensitivity and selectivity, and high specific surface area to comprehensively improve the gas sensing performance or use the synergistic effect between these materials and MoS_2 to achieve the goal of gas sensing. Chen *et al.*[112] synthesized 2D/0D MoS_2/ZnS heterostructures, which achieved the highly sensitive and recoverable detection of NO_2 at RT. The recovery time of the composite sensor to 5 ppm NO_2 was 4.6 min, which was much shorter than that of bare MoS_2. The p–n heterojunction created between MoS_2 and ZnS could act as a charge transfer bridge during NO_2 adsorption and desorption. Besides, the enriched active sites of MoS_2, the synergistic effects between the two components promoted an enhancement in sensing properties.

Jaiswal *et al.*[111] employed CdTe quantum dots with high sensitivity to NO_2 gas at RT to decorate MoS_2 nanoworms. The composite sensor could efficiently achieve spill-over effects and change the electronic structure. Furthermore, the p–n heterojunction, synergistic effect, defective intersurfaces, and unique morphology with large specific surface area jointly facilitated the high and fast adsorption of NO_2 molecules.

Besides the above-mentioned MoS_2-based binary-structured composite gas sensors, MoS_2-based ternary-structured composites have also been designed to achieve ideal gas sensing performances due to their unique/novel muti-level hierarchical heterostructures and multiple synergistic effects.

In our previous work,[114] a novel two-dimensional $Ti_3C_2T_x$ MXene@TiO_2/MoS_2 heterostructure was synthesized for the efficient and selective detection of NH_3 at RT. Its morphology is shown in Fig. 8a, where MoS_2 nanosheets grew on the surface of MXene and rectangular TiO_2 particles were derived from MXene during the high-temperature hydrothermal process. It could be seen that the composite sensors (MTM) exhibited a higher NH_3 gas sensing response value compared to that of pristine MXene and MoS_2, as shown in Fig. 8b, and outstanding selectivity was exhibited by the MTM-2 composite sensor, as shown in Fig. 8c. Finally, we concluded that the enhancement in the gas sensing performance was ascribed to the unique morphology and p–n heterojunction of the ternary MXene@TiO_2/MoS_2 composite. Moreover, the insertion of TiO_2 expanded the interlayer spacing of the $Ti_3C_2T_x$ MXene and provided more reactive sites for NH_3 adsorption.

Ding *et al.*[115] constructed an MoS_2–rGO–Cu_2O (MG–Cu) ternary composite for the efficient detection of NO_2 at RT. The hollow Cu_2O nanospheres were anchored on the surface of MoS_2–rGO, and the TEM image of this composite is shown in Fig. 8d. The sensor exhibited 11- and 5-times higher sensing response values to 500 ppb NO_2 compared to pure MoS_2 and binary MoS_2–rGO, respectively (Fig. 8e). Besides, it

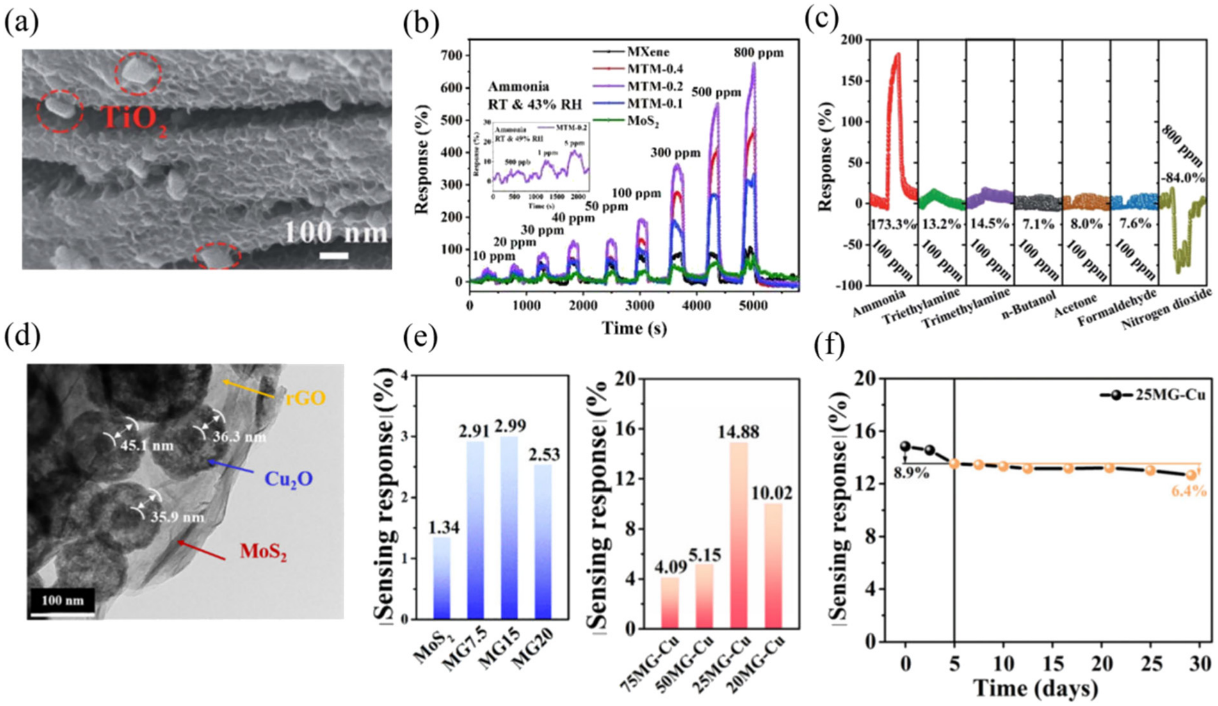

Fig. 8 (a) SEM images of $Ti_3C_2T_x$ MXene@TiO_2/MoS_2 (MTM-0.2). (b) Dynamic sensing characteristics of the prepared sensors to ammonia vapor at RT of 27 °C and RH of 43%. (c) Gas sensing responses of the $Ti_3C_2T_x$ MXene@TiO_2/MoS_2 (MTM-0.2)-based gas sensor for a concentration of 100 ppm of various gases at RT of 25 °C and RH of 41%. Reprinted with permission from ref. 114. Copyright 2022, The Royal Society of Chemistry. (d) TEM image of MoS_2–rGO–Cu_2O (MG–Cu) ternary composite. (e) Sensing response of MG and MG–Cu with different amounts of graphene to 500 ppb NO_2 at room temperature. (f) Stability of 25 MG–Cu sensor to 500 ppb NO_2 at room temperature. Reprinted with permission from ref. 115. Copyright 2021, Elsevier B.V.

also displayed excellent long-term stability (Fig. 8f). The superior sensing properties of this ternary composite sensor were mainly ascribed to the porous Cu_2O, which acted as a gas molecule permeation diffusion channel, while MoS_2–rGO acted as the bridge for electron transport. Meanwhile, the synergy of the shell-structure and heterojunction constructions among the three components contributed to the enhanced performance.

3. Categories of gas detected by MoS_2-based sensors

According to the discussion in the previous section, it can be seen that MoS_2-based gas sensors mainly show excellent recognition for NO_2 and NH_3 gases at RT. Alternatively, a few other gases can also be detected at RT such as nitric oxide (NO), hydrogen (H_2), ethanol, methanol, formaldehyde (HCHO), carbon monoxide (CO), sulfur dioxide (SO_2), benzene, acetone, and triethylamine (TEA), but the relevant reports are relatively scarce. In this case, it is worth exploring why MoS_2-based gas sensors can identify these gases, especially for NO_2 and NH_3 detection. In this section, we will classify the different gases detected by MoS_2-based gas sensors at RT and discuss their sensing mechanisms.

3.1 NO_2, NO, CO, and SO_2

NO_2 possesses high electrophilicity as an electron acceptor,[112] which means that it can easily trap electrons from the conduction band of sensing materials without high energies, causing an increase in the hole concentration of MoS_2 and a large change in the resistance of the sensor. Moreover, MoS_2 has more adsorption sites for NO_2 molecules. Regarding this, some theoretical calculation studies have verified the stronger affinity of MoS_2 for NO_2. Yue *et al.*[116] employed first-principles calculations to investigate the adsorption energy and charge transfer of various gas molecules such as H_2, O_2, H_2O, NH_3, NO, NO_2, and CO on monolayer MoS_2. They concluded that all the calculated gas molecules were physically adsorbed on the surface of MoS_2. However, regardless of the adsorption sites on MoS_2 including H site (top of the MoS_2 hexagon), T_S (top of S atoms) site, and B site (top of Mo–S bonds), NO_2 exhibited the highest adsorption energy and more charge transfer than other gases. Meanwhile, the H site was the most favorable adsorption site for H_2O, NH_3, and NO_2 molecules, resulting in adsorption energies of −234, −250, and −276 meV, respectively. Jiang *et al.*[117] also carried out the first-principles calculations to verify that perfect-layered MoS_2 (without vacancy) exhibited higher adsorption energies for N-based gas molecules such as NO and NO_2 compared with other gases. Meanwhile, this team also calculated the adsorption energies of NH_3, NO, and NO_2 adsorbed on defective MoS_2 with Mo vacancy and S vacancy. They found that the adsorption energies of NO and NO_2 on defective MoS_2 with Mo vacancy increased remarkably compared with perfect MoS_2. The electron localization function indicated that O–S and N–S covalent bonds were formed between NO and defective MoS_2, NO_2 and defective MoS_2, respectively, demonstrating that there was chemical adsorption between them.

Besides theoretical studies, experimental studies have also confirmed that there is strong interaction between NO_2 molecules and MoS_2. Ikram *et al.*[108] reported the preparation of a highly sensitive RT NO_2 sensor based on MoS_2/C_3N_4 hybrid material. They confirmed the presence of the Mo–N bond based on the high-resolution N 1s spectra of the MoS_2/C_3N_4 hybrid after absorbing NO_2, illustrating that Mo was a strong adsorption site for N-based gases.

The gas sensing mechanism of MoS_2-based gas sensors towards NO_2 at RT is mainly based on the Langmuir–Hinshelwood (adsorption–desorption) model.[118,119] Specifically, in an air atmosphere, the O_2 molecules surround the surface of MoS_2-based nanomaterials and extract free electrons from the conduction band of MoS_2 to form adsorbed oxygen species such as O_2^-, O^-, and O^{2-}. The equations describing this reaction are as follows:

$$O_{2(gas)} \rightarrow O_{2(ads)} \tag{1}$$

$$O_{2(ads)} + e^- \rightarrow O_{2ads}^- \tag{2}$$

$$O_{2ads}^- + e^- \rightarrow 2O_{ads}^- \tag{3}$$

$$O_{ads}^- + e^- \rightarrow O_{ads}^{2-} \tag{4}$$

However, the oxygen ion O_2^- is predominant at low temperature (RT∼150 °C).[120] The formation of O_2^- results in a high baseline resistance for n-type MoS_2 or low baseline resistance for p-type MoS_2. When introducing NO_2 on the surface of MoS_2, the oxidising gas further captures electrons from MoS_2 to form NO_2^-, and more holes accumulate in the conduction band of MoS_2, causing a higher resistance for n-type MoS_2 or lower resistance for p-type MoS_2. Meanwhile, the NO_2 gas will also react with O_2^- to generate NO_3^-. When an MoS_2-based sensor is put into an air atmosphere again, NO_2^- and NO_3^- would desorb and the released electrons come back to MoS_2, and thus the resistance will decrease for n-type MoS_2 or increase for p-type MoS_2 again. The reaction is as follows:

$$NO_{2(gas)} + e^- \rightarrow NO_{2ads}^- \tag{5}$$

$$2NO_{2(gas)} + O_{2ads}^- + e^- \rightarrow 2NO_{3ads}^- \tag{6}$$

$$NO_{2ads}^- + 2NO_{3ads}^- \rightarrow 3NO_{2(gas)} + O_{2(gas)} + e^- \tag{7}$$

In the case of NO gas, it is also an electron acceptor and easily oxidized into NO_2 gas in air. Although some theoretical studies show that the adsorption interaction of MoS_2 for NO is weaker than that of NO_2, there is also chemical adsorption and significant charge transfer between it and MoS_2, as confirmed by density of states analysis.[46] To date, NO room-temperature gas sensors based on MoS_2 have also been reported, and the sensing mechanism is according to the following equations:

$$NO_{(gas)} + e^- \rightarrow NO_{ads}^- \quad (8)$$

$$NO_{ads}^- + O_{2ads}^- + e^- \rightarrow NO_{(gas)} + O_{2ads}^- \quad (9)$$

When MoS_2-based gas sensors are exposed to NO gas, the reduction reaction of NO occurred, as shown in eqn (8), which leads to an increase in resistance for n-type MoS_2. Once the NO gas is withdrawn, the electrons return from NO_{ads}^- to MoS_2, resulting in a decrease in the resistance of MoS_2.

In addition to NO_2 and NO gases, CO and SO_2 can also be detected by MoS_2-based gas sensors at RT, but there are not many reports in this regard. Their sensing mechanisms are the same as NO_2 and NO on the surface of MoS_2, which is based on the interaction between absorbing oxygen and gas molecules to release electrons, leading to a change in the resistance of MoS_2. Zhang *et al.*[121] reported the preparation of a highly sensitive Ag-loaded ZnO/MoS_2 ternary nanocomposite room-temperature CO sensor. They described the sensing reaction by eqn (10), as follows:

$$CO + O_{ads}^- \rightarrow CO_2 + e^- \quad (10)$$

When the sensor was exposed to CO, its resistance decreased due to the release of electrons. The presence of noble metal Ag with catalytic activity accelerated the reaction.

Zhang *et al.*[122] demonstrated that Ni-doped MoS_2-based gas sensors exhibited an excellent SO_2 sensing performance at RT. The Ni-doped MoS_2 system had strong electrochemical

Table 1 A summary of MoS_2-based room-temperature NO_2 gas sensors

Materials	Gases	Concentration (ppm)	Response (R_a/R_g, R_g/R_a) or [($\Delta R/R$) × 100%]	Response/recovery time (s)	Ref./year
MoS_2 nanowires	NO_2	5	~10.5%	Incomplete recovery	30/2018
Vertically aligned MoS_2 on SiO_2 nanorod	NO_2	50	390%	Incomplete recovery	124/2018
MoS_2 monolayer	NO_2	0.02	20%	~/12 h	125/2014
MoS_2 bilayer film	NO_2	100	26.4%	11.3/5.3 min	126/2017
MoS_2 nanosheets	NO_2	5	88%	85/1420	127/2021
MoS_2 vertically aligned layers	NO_2	100	10%	Not recovered	128/2015
Vertically aligned MoS_2 flake	NO_2	50	~48.32%	98/not recovered	129/2018
		1	~3.4%	68/not recovered	
MoS_2 nanoflowers	NO_2	5	~59%	125/485	34/2020
MoS_2 flakes (UV light-activated)	NO_2	100	27.92%	29/350	130/2017
MoS_2 nanosheets (UV light-activated)	NO_2	5	~1.15	Complete recovery	73/2019
Au/MoS_2 (visible light-enhanced)	NO_2	1	8.1	~/27	131/2021
La/MoS_2	NO_2	10	45.34%	89.1/95.4	132/2020
Co/MoS_2	NO_2	100	51.08%	10/600	58/2022
Ni/MoS_2	NO_2	200	45.2%	28/250	133/2022
WO_3/MoS_2	NO_2	10	1.17	Complete recovery	78/2019
SnO_2/MoS_2	NO_2	5	18.7	74/complete recovery	77/2019
ZnO/MoS_2	NO_2	5	3050%	40/300	118/2018
In_2O_3/MoS_2	NO_2	1	39.4	72/118	79/2022
CuO/MoS_2 (red light-activated)	NO_2	10	~8	33.9/55.6	134/2022
MOF-In_2O_3/MoS_2	NO_2	10	9.36	152/179 (20 ppm)	135/2019
MoS_2@MoO_2	NO_2	100	~19	1.06/22.9	136/2019
PbS/MoS_2	NO_2	100	22.5%	30/235	109/2019
MoS_2/ZnS	NO_2	5	7.2	~/4.6 min	112/2021
CdTe/MoS_2	NO_2	10	~40%	16/114	111/2020
SnS_2/MoS_2	NO_2	100	~26	15.2/28.2	137/2020
WS_2/MoS_2	NO_2	0.02	26.12	1.6/27.7	91/2019
MoS_2/$Ti_3C_2T_x$ MXene	NO_2	100	65.6%	About 750/not recovered	101/2022
Ti_3C_2/MoS_2	NO_2	100	46.9	Incomplete recovery	95/2022
CTAB-MoS_2/rGO	NO_2	8	37.64%	Incomplete recovery	97/2022
$Mo_2Ti_3C_2T_x$/MoS_2	NO_2	50	415.8%	34.8/140.5	138/2022
MoS_2/C_3N_4	NO_2	30	~49	2.3/30.5	108/2020
MoS_2–rGO–Cu_2O	NO_2	0.5	14.8%	Incomplete recovery	115/2021
rGO/MoS_2	NO_2	40	25	160/3300	139/2018
$MoS_{2-x}Se_x$	NO	3	48%	410/340	140/2021
3D cone-shaped MoS_2 (UV light-activated)	NO	0.06	200%	130/~	68/2019
3D cone-shaped MoS_2 (white light-activated)	NO	0.06	75%	150/~	68/2019
MoS_2 monolayer (UV light-activated)	NO	100	25.63%	About 250/600	141/2019
CNFs/CoS_2/MoS_2	NO	50	19%	60/260 min	142/2020
MoS_2/Si nanowire array	NO	50	3518%	680/668	143/2017
Pt–ZnO/MoS_2	CO	5	5.08%	45/60	121/2017
Ni–MoS_2	SO_2	5	7.4%	50/56	122/2017
SnO_2/MoS_2 (UV light-activated)	SO_2	1	4.68	217/633	144/2021

activity due to the overlap of the conduction band and valence band, where the flow of electrons was easier from the valence band to conduction band. When the SO_2 and Ni-doped MoS_2 system interacted, the bond length values of the SO_2 molecules and the electronic structure of the Ni-doped MoS_2 system changed significantly, as verified by DFT calculation.

The sensing mechanism of MoS_2-based gas sensors towards SO_2 is based on eqn (11),[123] as follows:

$$SO_2 + O_{2ads}^- + e^- \rightarrow SO_3 + e^- \tag{11}$$

Table 1 summarizes the MoS_2 nanomaterial-based gas sensors for the detection of NO_2, NO, CO, and SO_2 gases at RT in recent years. It can be seen that there are more reports focused on the detection of NO_2 rather than NO, CO, and SO_2, illustrating that MoS_2 has a strong interaction for N-based gases. In addition, it is difficult for pristine MoS_2 NO_2 sensors to recovery completely, and thus several modification strategies have greatly improved their response and recovery rate to a certain extent.

3.2 NH_3

In contrast to NO_2, NH_3 gas is a well-known electron donor owing to the fact that it contains a pair of lone electrons, which are not involved in bonding. Therefore, the electron concentration will increase for the n-type MoS_2 sensing layer when exposed to NH_3, resulting in a low resistance. The adsorption energies of CO, NO_2, and NH_3 on pristine MoS_2 were analyzed by DFT calculation.[145] The results showed that the most stable adsorption energies for CO, NO_2, and NH_3 were 0.008, −0.131, and −0.217 eV, respectively, implying that the high interaction between NH_3 and MoS_2. The low positive value of 0.008 indicated that CO on MoS_2 was exothermic, unstable, and weakly adsorbed. Zhao *et al.*[146] also employed DFT calculation to investigate the adsorption energies of O_2, NO, NO_2, and NH_3 gas molecules on pristine MoS_2. They found that the adsorption energies values of O_2, NO, NO_2, and NH_3 gases on MoS_2 were 0.013, 0.026, 0.037, and 0.041 eV, respectively. Although all these gases exhibited weak physical adsorption interaction on MoS_2, obviously, NH_3 had the highest.

Sharma *et al.*[147] and Singh *et al.*[148] verified the high sensitivity of MoS_2 to NH_3 gas at RT *via* experimental measurements. Another important parameter involved is the response/recovery time, and these researchers observed that the pristine MoS_2-based NH_3 sensors showed a fast response/recovery time of 22/32 s towards 100 ppm NH_3 and 75/130 s towards 50 ppm NH_3, indicating that a fast and complete recovery can be achieved when NH_3 gas was detected.

The gas sensing mechanism of the MoS_2-based gas sensor towards NH_3 at RT is also based on the adsorption–desorption theory. The following equations are used to describe the interaction between NH_3 and the MoS_2 sensing layer.

$$4NH_3 + 5O_{2ads}^- \rightarrow 4NO + 6H_2O + 5e^- \tag{12}$$

When MoS_2 sensors are exposed to the reducing NH_3 gas, the NH_3 molecules will react with O_{2ads}^- to form NO and H_2O accompanied by the release of electrons; meanwhile, NH_3 molecule itself contains lone pair electrons, which makes more electrons return to the conduction band of MoS_2, causing a large change in resistance.

To further improve the gas sensing performance of MoS_2-based gas sensors to NH_3 at RT, several MoS_2 nanocomposite NH_3 gas sensors have been proposed in recent years. Table 2 presents a summary of MoS_2 nanomaterial-based gas sensors for the detection of NH_3 gas at RT.

Table 2 A summary of MoS_2-based room-temperature NH_3 gas sensors

Materials	Concentration (ppm)	Response (R_a/R_g, R_g/R_a) or [($\Delta R/R$) × 100%]	Response/recovery time (s)	Ref./year
NiO/MoS_2	10	63%	160/117 (20 ppm)	84/2019
MoS_2/CuO	100	∼47%	17/26	82/2018
MoS_2 nanostructure	50	10%	75/130	148/2020
MoS_2 thin film	100	2.2	22/32	137/2018
MoS_2/ZnO	50	46.2%	10/11	149/2017
MoS_2/Co_3O_4	5	∼65%	98/100	89/2017
MoS_2/MWCNTs	100	∼42%	80/90 (50 ppm)	106/2021
SnO_2/MoS_2	50	91.26	23/1.6	33/2020
MoS_2/MWCNT	150	∼26%	65/70	150/2020
Co_3O_4/MoS_2	50	4.2	105/353	83/2022
MoS_2/SnO_2	50	53%	Complete recovery	151/2021
PANI/MoS_2/SnO_2	100	10.9	21/130	152/2021
MoS_2 nanochains	200	40%	80/70	153/2022
P3HT/MoS_2	4	8%	100/500	107/2016
MoS_2/MoO_3	50	∼54%	45/53	154/2021
PANI/MWCNTs/MoS_2	5	40.12%	56/50	155/2018
PANI/MoS_2	5	10.94%	98/57	155/2018
$Ti_3C_2T_x$ MXene@TiO_2/MoS_2	100	163.3%	117/88	114/2022

3.3 H_2

H_2 as an abundant, green and renewable energy source has been used in various fields such as fuel cells, automobiles, and power plants.[156] Moreover, it is also applied in the chemical industry, nuclear reactors, petroleum extraction, and semiconductor processing.[157] However, H_2 is also associated with many potential safety hazards duo to its explosive and flammable nature.[158] Especially when its concentration is higher than 4% in the atmosphere, an explosion will occur. Therefore, the efficient detection of H_2 is particularly important. Currently, although SMO H_2 sensors exhibit high gas sensing response values, their high operating temperature also brings hidden dangers to a certain extent because the explosive limit of H_2 is easily reached at a high temperature. Thus, the detection of H_2 at low or room temperature will greatly improve the safety. To date, many low or room-temperature H_2 sensors based on MoS_2 have been reported. Theoretically, MoS_2 is not sensitive to nonpolar molecules of H_2.[159] Bollinger *et al.*[160] believed that the edges of MoS_2 behave like metallic inter-connecting wires for the adsorption of H_2 at RT. Dolui *et al.*[161] and Gomez *et al.*[162] also proposed that H_2 behaves as an electron acceptor, which is favourable for absorption along the edges of MoS_2 flakes. To date, the main approach employed to increase the sensitivity of MoS_2 to H_2 is its functionalization with noble metals including Au, Ag, Pt, and Pd. Zhang *et al.*[163] investigated the effect of different noble metals (Cu, Au, Ag, Pt, and Pd) decorated on monolayer MoS_2 on its hydrogen sensing performances by first principles. They concluded that the introduction of all the noble metals had a positive effect on H_2 adsorption, which contributed to the hybridization of the noble metal d, S p, Mo d and H s orbitals. Especially Pt and Pd could enhance the adsorption interaction and increase the charge transfer between H_2 molecules and monolayer MoS_2. Some experimental studies are also consistent with the theoretical results. Baek *et al.*,[164] Jaiswal *et al.*[49] and Mai *et al.*[165] used Pd to functionalize MoS_2 and realize the detection of H_2 at RT. The former research groups suggested that the mechanism of H_2 sensing on Pd/MoS_2 is ascribed to the electron transfer from MoS_2 and Pd in air due to the lower work function of MoS_2 than Pd. Alternatively, the formation of Pd-hydride (PdHx) on Pd surface when exposed to H_2 resulted in electron transfer in the opposite direction from PdHx to MoS_2, resulting in a change in sensor resistance. The latter research group concluded that the deposition of Pd nanoclusters on MoS_2 caused p-type semiconductor behavior in the Pd/MoS_2 composite. Meanwhile, the strong affinity of Pd provided more favorable adsorption sites for H_2 molecules and initiated their chemical reactions.

Besides the use of noble metals to trigger the sensitive response of MoS_2 to H_2 at RT, another strategy is to compound some potential materials that respond to H_2, such as MoO_3,[166] graphene,[167] and SnO_2 (ref. 168) with MoS_2 as suitable templates or supports. Table 3 displays the MoS_2 nanomaterial-based gas sensors for H_2 gas detection at RT. The sensing mechanism can be explained based on the interaction between H_2 molecules and O_{2ads}^-. The whole reaction can be given by the following equations:

$$H_{2(gas)} \rightarrow H_{2(ads)} \tag{13}$$

$$H_{2(ads)} \rightarrow 2H_{(ads)} \tag{14}$$

$$2H_{(ads)} + O_{2ads}^- \rightarrow H_2O + e^- \tag{15}$$

3.4 Other VOCs

The other VOC gases that can be detected by MoS_2-based gas sensors at RT include ethanol, methanol, formaldehyde (HCHO), and benzene. VOCs gases, as reducing agents, present electron-donating characteristics similar to NH_3. To date, there are a few reports on the detection of these gases at RT by MoS_2-based sensing devices, which mainly consider the activity, electronic characteristics, molecular size of the

Table 3 A summary of MoS_2-based room-temperature H_2 gas sensors

Materials	Concentration (ppm)	Response (R_a/R_g, R_g/R_a) or [($\Delta R/R$) × 100%]	Response/recovery time (s)	Ref./year
MoS_2/Cs_xWO_3	500	50.6%	60/120	169/2022
UNCD/MoS_2/ZnO	100	50.3%	8/12	170/2019
Bulk-MoS_2	100	14.2%	28/42	171/2019
Pd–MoS_2/Si	1%	~53.3%	~13.1/15.03 min	164/2017
RGO/MoS_2	200	~1.1%	~	172/2017
Pd–SnO_2/MoS_2	5000	18%	30/19	173/2017
Pd/MoS_2 (light-activated)	140	17.45 ± 1.02%	351/515 (120 ppm)	165/2021
Pd/MoS_2	500	33.7%	16/38	49/2020
Vertically aligned MoS_2/Si	100	685.7%	109/102	174/2016
Edge-oriented MoS_2 flake	10 000	1%	14.3/137	175/2017
MoS_2/GaN	5%	~25%	~	110/2019
Zn-doped MoO_3/MoS_2	500	28.91%	24.6/18.5	176/2022
MoS_2/graphene	1000	8.1%	32/33	177/2022
MoS_2/ZnO	500	51.5%	14/19	178/2021

Table 4 A summary of MoS_2-based room-temperature ethanol, methanol, formaldehyde, and benzene gas sensors

Materials	Gases	Concentration (ppm)	Response (R_a/R_g, R_g/R_a) or [($\Delta R/R$) × 100%]	Response/recovery time (s)	Ref./year
CeO_2/MoS_2	Ethanol	50	7.78	7/5	75/2021
α-Fe_2O_3/MoS_2	Ethanol	100	88.9%	6/5 (30 ppm)	183/2018
Fe–TiO_2/MoS_2	Ethanol	5	150%	62/49 (1 ppm)	179/2018
Ag/MoS_2	Methanol	100	21.6%	240/1100	50/2021
In_2O_3/MoS_2	Formaldehyde	50	75.2%	14/22	185/2018
rGO/MoS_2	Formaldehyde	10	~2.7%	73/~	184/2017
rGO/MoS_2	Formaldehyde	10	4.8%	~	186/2017
rGO/MoS_2 (visible-light activated)	Formaldehyde	10	64%	79/17	72/2021
Pd–TiO_2/MoS_2	Benzene	50	64%	13/10	182/2018

gas itself, and the affinity of sensitive materials to gas molecules.

Wu *et al.*[179] prepared an Fe–TiO_2/MoS_2 composite film ethanol RT sensor. They proposed that Fe ion doping can optimize the electrical property of the sensing material. The sensor was sensitive to ethanol, which was attributed to the fact that the hydroxyl in the rotating ethanol molecule faced the Fe–TiO_2 substrate and elongation of the C–O and H–O bonds on the adsorption surface of Fe–TiO_2, which resulted in a shorter adsorption distance and higher adsorption strength. The density of states revealed that there was strong adsorption interaction between ethanol and Fe–TiO_2 due to the large shift in the energy level of the Fe 3d and O 2p orbitals after adsorption. Finally, combined with the p–n heterojunctions generated at the interface of n-type Fe–TiO_2 and p-type MoS_2, the sensing response to ethanol was stronger.

Chakraborty *et al.*[180] analyzed the highly selective methanol sensing mechanism of electrodeposited pristine MoS_2 using first principle analysis. They found that although the electron-donating capability and charge transfer of 2-propanol and ethanol were higher than that of methanol, the smaller dimension of methanol, two favorable adsorption sites (Ori-A and Ori-B) of methanol on MoS_2 surface, and approximately 20-times larger adsorption energy than that of ethanol and 2-propanol were the main reasons for the high sensitivity of MoS_2 towards the detection of methanol.

Actually, pristine MoS_2 does not have good sensitivity to formaldehyde, although it is a small molecule. Deng *et al.*[181] employed DFT to investigate the adsorption of formaldehyde on Ni-, Pt-, Ti- and Pd-doped monolayer MoS_2, respectively. They found that Ti–MoS_2 was the dominant one in terms of adsorption energy. Moreover, the projected density of states (PDOS) and charge transfer indicate that the interaction between the formaldehyde molecule and Ti dopant was chemisorption *via* the Ti–O bond, illustrating that Ti–MoS_2 may be suitable for the detection of formaldehyde. In addition, some compounds based on MoS_2 can also be sensitive to formaldehyde, but the mechanism of their sensitivity has not been clearly defined.

Zhang *et al.*[182] reported that a Pd–TiO_2/MoS_2 composite sensor showed selectivity and sensitivity towards benzene at RT. The sensing mechanism could be ascribed to the fact that Pd in TiO_2/MoS_2 has catalytic interaction toward benzene with a C–H bond and the synergistic effect of the ternary nanostructures, which can facilitate effective charge transport.

The following equations describe the reactions between the oxygen ion O_2^- created on the surface of MoS_2-based sensing materials and ethanol, methanol, formaldehyde, and benzene molecules, respectively.[183,184]

$$C_2H_5OH_{(ads)} + 3O_{2ads}^- \rightarrow 2CO_2 + 3H_2O + 6e^- \tag{16}$$

$$2CH_3OH_{(ads)} + 3O_{2ads}^- \rightarrow 2CO_2 + 4H_2O + 3e^- \tag{17}$$

$$HCHO_{(ads)} + O_{2ads}^- \rightarrow CO_2 + H_2O + e^- \tag{18}$$

$$C_6H_{6(ads)} + 15O_{2ads}^- \rightarrow 12CO_2 + 6H_2O + 15e^- \tag{19}$$

Table 4 presents a summary of the MoS_2 nanomaterial-based gas sensors for the detection of ethanol, methanol, formaldehyde, and benzene gases at RT.

4. Conclusions and outlook

Obviously, MoS_2 exhibits great capabilities in the field of gas sensing, especially for room-temperature gas detection. In this review, firstly, the strategies for improving the gas sensing performance of MoS_2 were introduced. Subsequently, the different types of gases that can be detected by MoS_2-based gas sensors at room temperature were proposed and classified. Meanwhile, the sensing mechanisms of MoS_2-based gas sensors towards different gases were also analyzed.

Pristine MoS_2 gas sensors exhibit low gas sensing response values and incomplete recovery problems at room temperature, which are unfavorable for gas detection. Consequently, various strategies have been developed for improving the gas sensing performance of MoS_2 based gas sensors including morphology design, creating sulfur vacancies, decorating with noble metals, doping elements, light assistance, and construction of composites. Although the morphology design of MoS_2 involves multiple patterns such as quantum dots, nanowires, nanosheets, and nanoflowers, each morphology exhibits unique physical and chemical properties and gas sensing performance characteristics, and the key issue of incomplete recovery has not been well solved. The vacancies in MoS_2 belong to high energy binding sites, especially S vacancies as active sites to enhance the gas molecules adsorption. However, this high adsorption capacity will also result in a slow response and recovery rate. The decoration of the surface of MoS_2 with noble metals can assist in overcoming the problem of selectivity to a certain extent due to the fact that noble metals possess affinity for some specific gas molecules. Element doping can address the challenge of sluggish sensing of MoS_2 at room temperature owing to the adjustable active sites and electrical property. To date, doping strategies focus on theoretical calculations based on density functional theory, while experimental studies are rare. The light-assisted strategies include UV-light and visible-light activation. The power of these two lights is different, resulting in optoelectronic and photocatalytic gas sensing mechanisms, respectively, which accelerates the chemisorption reaction and causes a large change in the resistance of the sensor upon exposure to gases. Room-temperature MoS_2 nanocomposite gas sensors are the most studied at present. The construction of composites of MoS_2 (binary or ternary) can be considered one of the most effective modification methods to address the low gas sensing response and delayed recovery time of pristine MoS_2 gas sensors. The heterojunctions and synergistic effects created by the different components are conducive to improve their comprehensive gas sensing performance. Especially the high electrical conductivity, unique electronic transfer channels, and similar sensitive selectivity are observed in nanocomposites.

According to the reports on the detection of several gases by MoS_2-based gas sensors at room temperature such as NO_2, NO, SO_2, CO, NH_3, H_2, ethanol, methanol, formaldehyde, and benzene, MoS_2 seems show strong adsorption interaction for N-based gases such as NO_2 and NH_3. NO_2 as an electron acceptor exhibits high electrophilicity, which can easily trap electrons from the conduction band of MoS_2. In contrast to NO_2, NH_3 acts as an electron donor with a pair of lone electrons that can give more electrons to MoS_2, and thus the resistance of MoS_2 sensors change greatly. Besides NO_2 and NH_3, H_2 can also be detected by MoS_2-based gas sensors at room temperature. Several researchers have proposed that H_2 in nature favor absorption along the edges of MoS_2, which behave like metallic inter-connecting wires to attract H_2 at RT. The detection of other VOC gases such as ethanol, methanol, formaldehyde, and benzene by MoS_2 nanocomposite gas sensors has also been reported, which is mainly related to the strong force on these gases at one of the special adsorption sites in the composites. To date, the sensing mechanisms of MoS_2-based gas sensors for the above-mentioned gases are mainly based on the adsorption/desorption theories. The target gases react with the adsorbed oxygen ions O_{2ads}^- and release electrons to the conduction band of MoS_2, resulting in a change in resistance and sensitive response.

Although the above-mentioned strategies have made great progress to improve the gas sensing properties of MoS_2-based gas sensors at room temperature, there are still some interesting research directions and challenges that deserve to be explored.

Firstly, besides the strong interaction between MoS_2 and gas molecules, the deeper reasons for the slow or incomplete recovery of MoS_2 sensors to gases need to be investigated. The transduction mechanism, intrinsic characteristics, and desorption reaction seem to affect the recovery rate. In addition, NH_3 is more easily desorbed from the surface of MoS_2 than NO_2 in the case of the same N-based gases, which is worth further discussion. Secondly, the gas sensing response, selectivity, and long-term stability of MoS_2-based gas sensors are still unsatisfactory. Therefore, novel MoS_2-based room temperature gas sensors should receive more attention. Some strategies such as adjusting the active sites of MoS_2 from basal plane to edges, constructing advanced structured MoS_2 nanocomposites, and optimizing the fabrication process of devices may be interesting points. Finally, the gas sensing mechanisms of MoS_2 materials not only depend on the theories of adsorption–desorption and charge carrier transport, where the whole reactive process is complicated, and thus more crucial interactions between MoS_2 and gas molecules need to be further studied.

Conflicts of interest

There are no conflicts to declare.

Acknowledgements

This work was supported by the National Natural Science Foundation of China (No. 41876055 and 61761047), the Yunnan Provincial Department of Science and Technology through the Key Project for the Science and Technology (Grant No. 2017FA025), Program for Innovative Research Team (in Science and Technology) in University of Yunnan Province, and Project of the Department of Education of Yunnan Province (2022Y003).

References

1 Y. Zhou, X. Li, Y. J. Wang, H. L. Tai and Y. C. Guo, *Anal. Chem.*, 2019, **91**, 3311–3318.

2 T. Jarvinen, G. S. Lorite, J. Perantie, G. Toth, S. Saarakkala, V. K. Virtanen and K. Kordas, *Nanotechnology*, 2019, **30**, 405501.

3 Y. J. Wang, Y. Zhou, Y. H. Wang, R. J. Zhang, J. Li, X. Li and Z. G. Zang, *Sens. Actuators, B*, 2021, **349**, 130770.

4 M. Sajjad and P. Feng, *Mater. Res. Bull.*, 2014, **49**, 35–38.

5 Y. Zhou, Y. H. Wang, Y. J. Wang, H. C. Yu, R. J. Zhang, J. Li, Z. G. Zang and X. Li, *ACS Appl. Mater. Interfaces*, 2021, **13**, 56485–56497.

6 M. Barzegar and B. Tudu, *Surf. Innovations*, 2018, **6**, 205–230.

7 Q. Li, J. P. Meng and Z. Li, *J. Mater. Chem. A*, 2022, **10**, 8107–8128.

8 X. H. Liu, T. T. Ma, N. Pinna and J. Zhang, *Adv. Funct. Mater.*, 2017, **27**, 1702168.

9 T. H. Kim, Y. H. Kim, S. Y. Park and H. W. Jang, *Chemosensors*, 2017, **5**, 15.

10 G. Neri, *Chemosensors*, 2017, **5**, 21.

11 R. Kumar, N. Goel, M. Hojamberdiev and M. Kumar, *Sens. Actuators, A*, 2020, **303**, 111875.

12 K. F. Mak, C. Lee, J. Hone, J. Shan and T. F. Heinz, *Phys. Rev. Lett.*, 2010, **105**, 136805.

13 G. C. Lu, X. H. Liu, W. Zheng, J. Y. Xie, Z. S. Li, C. M. Lou, G. L. Lei and J. Zhang, *Rare Met.*, 2022, **41**(5), 1520–1528.

14 Y. S. Xu, J. Y. Xie, Y. F. Zhang, F. H. Tian, C. Yang, W. Zheng, X. H. Liu, J. Zhang and N. Pinna, *J. Hazard. Mater.*, 2021, **411**, 125120.

15 A. V. Agrawal, R. Kumar, S. Venkatesan, A. Zakhidov, G. Yang, J. M. Bao, M. Kumar and M. Kumar, *ACS Sens.*, 2018, **3**, 998–1004.

16 C. Yang, J. Y. Xie, C. M. Lou, W. Zheng, X. H. Liu and J. Zhang, *Sens. Actuators, B*, 2021, **333**, 129571.

17 M. Kumar, A. V. Agrawal, M. Moradi and R. Yousefi, *Nanomater. Air Rem.*, 2020, 107–130, DOI: 10.1016/B978-0-12-818821-7.00006-3.

18 A. V. Agrawal, N. Kumar and M. Kumar, *Nano-Micro Lett.*, 2021, **13**, 305–362.

19 Q. Y. He, Z. Y. Zeng, Z. Y. Yin, H. Li, S. X. Wu, X. Huang and H. Zhang, *Small*, 2012, **8**, 2994–2999.

20 S. M. Cui, Z. H. Wen, X. K. Huang, J. B. Chang and J. H. Chen, *Small*, 2015, **11**, 2305–2313.

21 B. Radisavljevic, A. Radenovic, J. Brivio, V. Giacometti and A. Kis, *Nat. Nanotechnol.*, 2011, **6**, 147–150.

22 K. Y. Ko, J. G. Song, Y. Kim, T. Choi, S. Shin and C. W. Lee, *ACS Nano*, 2016, **10**, 9287–9296.

23 M. Kan, J. Y. Wang, X. W. Li, S. H. Zhang, Y. W. Li, Y. Kawazoe, Q. Sun and P. Jena, *J. Phys. Chem. C*, 2014, **118**, 1515–5122.

24 D. Voiry, A. Mohiteb and M. Chhowalla, *Chem. Soc. Rev.*, 2015, **44**, 2702–2712.

25 R. Kumar, W. Zheng, X. H. Liu, J. Zhang and M. Kumar, *Adv. Mater. Technol.*, 2020, **5**, 1901062.

26 W. Zheng, X. H. Liu, J. Y. Xie, G. C. Lu and J. Zhang, *Coord. Chem. Rev.*, 2021, **447**, 214151.

27 A. Hermawan, N. L. W. Septiani, A. Taufik, B. Yuliarto, Suyatman and S. Yin, *Nano-Micro Lett.*, 2021, **13**, 207.

28 Z. X. Gan, L. Z. Liu, H. Y. Wu, Y. L. Hao, Y. Shan, X. L. Wu and P. K. Chu, *Appl. Phys. Lett.*, 2015, **106**, 233113.

29 Y. Niu, W. C. Jiao, R. G. Wang, G. M. Ding and Y. F. Huang, *J. Mater. Chem. A*, 2016, **4**, 8198–8203.

30 R. Kumar, N. Goel and M. Kumar, *Appl. Phys. Lett.*, 2018, **112**, 053502.

31 D. J. Late, Y. K. Huang, B. Liu, J. Acharya, S. N. Shirodkar, J. J. Luo, A. M. Yan, D. Charles, U. V. Waghmare and V. P. Dravid, *ACS Nano*, 2013, **7**, 4879–4891.

32 W. L. Li, Y. Zhang, X. Long, J. X. Cao, X. Xin, X. X. Guan, J. F. Peng and X. J. Zheng, *Sensors*, 2019, **19**, 2123.

33 W. X. Wang, Y. H. Zhen, J. Y. Zhang, Y. D. Li, H. Zhong, Z. L. Jia, Y. Xiong, Q. Z. Xue, Y. G. Yan and N. S. Alharbi, *Sens. Actuators, B*, 2020, **321**, 128471.

34 N. T. Thang, L. T. Hong, T. H. Nguyen, C. M. Hung, N. V. Duy, N. V. Hieu and N. D. Hoa, *RSC Adv.*, 2020, **10**, 12759–12771.

35 H. Long, A. Harley-Trochimczyk, T. Pham, Z. Tang, T. Shi, A. Zettl, C. Carraro, M. A. Worsley and R. Maboudian, *Adv. Funct. Mater.*, 2016, **26**, 5158–5165.

36 J. H. Hong, Z. X. Hu, M. Probert, K. Li, D. H. Lv, X. N. Yang, L. Gu, N. N. Mao, Q. L. Feng and L. M. Xie, *Nat. Commun.*, 2015, **6**, 6293.

37 H. Y. Nan, Z. L. Wang, W. H. Wang, Z. Liang, Y. Lu, Q. Chen, D. W. He, P. H. Tan, F. Miao and X. R. Wang, *ACS Nano*, 2014, **8**, 5738–5745.

38 Z. Y. Qin, K. Xu, H. C. Yue, H. Wang, J. Zhang, C. Ouyang, C. S. Xie and D. W. Zeng, *Sens. Actuators, B*, 2018, **262**, 771–779.

39 D. Burman, R. Ghosh, S. Santra, S. K. Ray and P. K. Guha, *Nanotechnology*, 2017, **28**, 435502.

40 R. Kumar, N. Goel, A. V. Agrawal, R. Raliya, S. Rajamani, G. Gupta, P. Biswas, M. Kumar and M. Kumar, *IEEE Sens. J.*, 2020, **19**, 10214–10220.

41 H. X. Li, M. Huang and G. Y. Cao, *Phys. Chem. Chem. Phys.*, 2016, **21**, 15110–15117.

42 X. W. Chen, J. Shi, T. Wang, S. Y. Zheng, W. Lv, X. Y. Chen, J. H. Yang, M. Zeng, N. T. Hu and Y. J. Su, *ACS Sens.*, 2022, **7**, 816–826.

43 Y. Xia, C. Y. Hu, S. H. Guo, L. B. Zhang, M. J. Wang, J. H. Peng, L. Xu and J. Wang, *ACS Appl. Nano Mater.*, 2020, **3**, 665–673.

44 H. P. Komsa, J. Kotakoski, S. Kurasch, O. Lehtinen, U. Kaiser and A. V. Krasheninnikov, *Phys. Rev. Lett.*, 2012, **109**, 035503.

45 L. C. Zhang, Y. Y. Liang, L. M. Yu, H. J. Wang and M. L. Yin, *Sens. Actuators, B*, 2022, **359**, 131539.

46 F. F. Li and C. M. Shi, *Appl. Surf. Sci.*, 2018, **434**, 294–306.

47 X. Tian, X. X. Cui, T. R. Lai, J. R. Z. C. Yang, M. J. Xiao, B. S. Wang, X. C. Xiao and Y. D. Wang, *Nano Mater. Sci.*, 2021, **3**, 390–403.

48 N. Sakhuja, A. Gupta, R. Jha and N. Bhat, *J. Alloys Compd.*, 2022, **899**, 163166.

49 J. Jaiswal, P. Tiwari, P. Singh and R. Chandra, *Sens. Actuators, B*, 2020, **325**, 128800.

50 P. Halvaee, S. Dehghani and M. Mohammadzadeh, *IEEE Sens. J.*, 2021, **21**, 4233–4240.

51 J. Park, J. H. Mun, J. S. Shin and S. W. Kang, *R. Soc. Open Sci.*, 2019, **5**, 181462.

52 H. Peng, J. Lu, C. X. Wu, Z. X. Yang, H. Chen, W. J. Song, P. Q. Li and H. Z. Yin, *Appl. Surf. Sci.*, 2015, **353**, 1003–1012.

53 C. Liu, Y. Zhang, J. Y. Hu, J. X. Ren, Y. Q. Song, J. F. Peng, M. Ma and J. J. Tan, *Mater. Lett.*, 2020, **273**, 127961.

54 S. G. Ramaraj, S. Nundy, P. Zhao, D. Elamaran, A. A. Tahir, Y. Hayakawa, M. Muruganathan, H. Mizuta and S. W. Kim, *ACS Omega*, 2022, **7**, 10492–10501.

55 Z. Xiao, W. Wu, X. W. Wu and Y. F. Zhang, *Chem. Phys. Lett.*, 2020, **755**, 137768.
56 W. J. Hou, H. W. Mi, R. C. Peng, S. D. Peng, W. Zeng and Q. Zhou, *Nanomaterials*, 2021, **11**, 314.
57 R. Y. Zhang, D. Fu, J. M. Ni, C. B. Sun and S. X. Song, *Chem. Phys. Lett.*, 2019, **715**, 273–277.
58 P. Bharathi, S. Harish, M. Shimomura, S. Ponnusamy, M. K. Mohan, J. Archana and M. Navaneethan, *Sens. Actuators, B*, 2022, **360**, 131600.
59 R. Z. Wu, J. Y. Hao, S. L. Zheng, Q. Sun, T. T. Wang, D. Zhang, H. Zhang, Y. Wang and X. Zhou, *Appl. Surf. Sci.*, 2021, **571**, 151162.
60 T. E. Gber, H. Louis, A. E. Owen, B. E. Etinwa, I. Benjamin, F. C. Asogwa, M. M. Orosun and E. A. Eno, *RSC Adv.*, 2022, **12**, 25992–26010.
61 A. Kazemi, M. Rodner, M. R. Fadavieslam, P. D. Kaushik, I. G. Ivanov, J. Eriksson, M. Syvajarvi, R. Yakimova and G. R. Yazdi, *Surf. Interfaces*, 2021, **25**, 101200.
62 J. Zhu, H. Zhang, Y. W. Tong, L. Zhao, Y. F. Zhang, Y. Z. Qiu and X. N. Lin, *Appl. Surf. Sci.*, 2017, **419**, 522–530.
63 E. Salih and A. I. Ayesh, *Phys. E*, 2021, **131**, 114736.
64 K. N. Ding, Y. H. Lin and M. Y. Huang, *Vacuum*, 2016, **130**, 146–153.
65 M. J. Szary, *Appl. Surf. Sci.*, 2021, **547**, 149026.
66 Y. Zhou, C. Zou, X. G. Lin and Y. C. Guo, *Appl. Phys. Lett.*, 2018, **113**, 082103.
67 J. Guo, R. M. Wen, J. Y. Zhai and Z. L. Wang, *Sci. Bull.*, 2019, **64**, 128–135.
68 Y. Z. Chen, S. W. Wang, C. C. Yang, C. H. Chung, Y. C. Wang, S. W. H. Chen, C. W. Chen, T. Y. Su, H. N. Lin, H. C. Kuo and Y. L. Chueh, *Nanoscale*, 2019, **11**, 10410–10419.
69 T. Pham, G. Li, E. Bekyarova, M. E. Itkis and A. Mulchandani, *ACS Nano*, 2019, **13**, 3196–3205.
70 P. C. Chen, S. Sukcharoenchoke, K. Ryu, L. G. Arco, A. Badmaev, C. Wang and C. Zhou, *Adv. Mater.*, 2010, **22**, 1900.
71 D. L. Wang, A. T. Chen and A. K. Y. Jen, *Phys. Chem. Chem. Phys.*, 2013, **15**, 5017–5021.
72 J. Wang, H. Y. Deng, X. Li, C. Yang and Y. Xia, *Sens. Actuators, B*, 2019, **304**, 127317.
73 Y. Kang, S. Pyo, E. Jo and J. Kim, *Nanotechnology*, 2019, **30**, 355504.
74 M. Donarelli, S. Prezioso, F. Perrozzi, F. Bisti, M. Nardone, L. Giancaterini, C. Cantalini and L. Ottaviano, *Sens. Actuators, B*, 2015, **207**, 602–613.
75 J. H. Zhang, T. T. Li, J. Y. Guo, Y. Q. Hu and D. Z. Zhang, *Appl. Surf. Sci.*, 2021, **568**, 150942.
76 X. Chang, X. F. Li, X. R. Qiao, K. Li, Y. X. Li, T. C. Guo, L. Zhu and Q. Z. Xue, *Sens. Actuators, B*, 2019, **304**, 127430.
77 Y. T. Han, Y. J. Ma, Y. Liu, S. S. Xu, X. W. Chen, M. Zeng, N. T. Hu, Y. J. Su, Z. H. Zhou and Z. Yang, *Appl. Surf. Sci.*, 2020, **493**, 613–619.
78 D. H. Baek, G. Choi, Y. Kwak, B. H. Cho and J. Kim, Proceedings of the IEEE International Conference on Micro Electro Mechanical Systems (MEMS), *2019 IEEE 32nd International Conference on Micro Electro Mechanical Systems, MEMS 2019*, 2019, pp. 468–471.
79 Y. N. Liu, S. Li, S. Xiao and K. Du, *Colloids Surf., A*, 2022, **648**, 129435.
80 P. X. Zhao, Y. Tang, J. Mao, Y. X. Chen, H. Song, J. W. Wang, Y. Song, Y. Q. Liang and X. M. Zhang, *J. Alloys Compd.*, 2016, **674**, 252–258.
81 R. Kumar, N. Goel, M. Mishra, G. Gupta, M. Fanetti, M. Valant and M. Kumar, *Adv. Mater. Interfaces*, 2018, **5**, 1800071.
82 S. Sharma, A. Kumar, N. Singh and D. Kaur, *Sens. Actuators, B*, 2018, **275**, 499–507.
83 Y. Xiong, W. D. Liu, K. C. Wu, T. Liu, Y. M. Chen, X. Z. Wang and J. Tian, *J. Alloys Compd.*, 2022, **927**, 166962.
84 D. Z. Zhang, Y. B. Jin and Y. H. Cao, *J. Mater. Sci.: Mater. Electron.*, 2019, **30**, 573–581.
85 Y. Q. Ding, X. Z. Guo, B. S. Du, X. F. Hu, X. Yang, Y. He, Y. Zhou and Z. G. Zang, *J. Mater. Chem. C*, 2021, **9**, 4838–4846.
86 H. Yan, M. J. Zhong, Z. Lv and P. B. Wan, *Small*, 2017, **13**, 1701697.
87 S. Ahmad, I. Khan, A. Husain, A. Khan and A. M. Asiri, *Polymer*, 2021, **12**, 3047.
88 X. Bai, H. Lv, Z. Liu, J. K. Chen, J. Wang, B. H. Sun, Y. Zhang, R. H. Wang and K. Y. Shi, *J. Hazard. Mater.*, 2021, **416**, 125830.
89 D. Z. Zhang, C. X. Jiang, P. Li and Y. E. Sun, *ACS Appl. Mater. Interfaces*, 2017, **9**, 6462–6471.
90 J. Sun, N. Lin, H. Ren, C. Tang, L. T. Yang and X. Zhao, *RSC Adv.*, 2016, **6**, 17494–17503.
91 M. Ikram, L. J. Liu, Y. Liu, L. F. Ma, H. Lv, M. Ullah, L. He, H. Y. Wu, R. H. Wang and K. Y. Shi, *J. Mater. Chem. A*, 2019, **7**, 14602–14612.
92 S. Dhara, H. Jawa, S. Ghosh, A. Varghese, D. Karmakar and S. Lodha, *ACS Appl. Mater. Interfaces*, 2021, **13**, 30785–30796.
93 S. H. Zhang, J. Y. Wang, N. L. Torad, W. Xia, M. A. Aslam, Y. V. Kaneti, Z. F. Hou, Z. J. Ding, B. Da and A. Fatehmulla, *Small*, 2019, **16**, 1901718.
94 G. Liu, S. L. Rumyantsev, C. Jiang, M. S. Shur and A. A. Balandin, *IEEE Electron Device Lett.*, 2015, **36**, 1202–1204.
95 V. Le, Y. Vasseghian, V. Doan, T. T. T. Nguyen, T. T. T. Vo, K. B. Vu, Q. H. Vu, T. D. Lam and V. A. Tran, *Chemosphere*, 2022, **291**, 133025.
96 R. Zen, Y. B. Shi, T. M. Song, T. Wang, B. L. Tang, H. D. Niu and X. Y. Yu, *Chemosphere*, 2022, **9**, 345.
97 W. B. Li, H. Li, R. Qian, S. J. Zhuo, P. F. Ju and Q. Chen, *Nanomaterials*, 2022, **12**, 1300.
98 C. Yang, Y. Y. Wang, Z. K. Wu, Z. B. Zhang, N. T. Hu and C. S. Peng, *Nanomaterials*, 2022, **12**, 901.
99 I. Jahangir, M. A. Uddin, A. K. Singh, M. V. S. Chandrashekhar and G. Koley, *IEEE Sens. J.*, 2021, **21**, 26549–26555.
100 W. Zheng, Y. S. Xu, L. L. Zheng, C. Yang, N. Pinna, X. H. Liu and J. Zhang, *Adv. Funct. Mater.*, 2020, **30**, 2000435.
101 H. Yan, L. H. Chu, Z. Li, C. X. Sun, Y. X. Shi and J. Ma, *Sensors and Actuators Reports*, 2022, **4**, 100103.
102 F. Schedin, A. K. Geim, S. V. Morozov, E. W. Hill, P. Blake, M. I. Katsnelson and K. S. Novoselov, *Nat. Mater.*, 2007, **6**, 652–655.

103 M. Sangeetha and D. Madhan, *Opt. Laser Technol.*, 2020, **127**, 106193.

104 J. D. Fowler, M. J. Allen, V. C. Tung, Y. Yang, R. B. Kaner and B. H. Weiller, *ACS Nano*, 2009, **3**, 301–306.

105 F. L. Meng, Z. Guo and X. J. Huang, *TrAC, Trends Anal. Chem.*, 2015, **68**, 37–47.

106 S. Singh and S. Sharma, *Mater. Today*, 2021, **45**, 4910–4913.

107 T. Xie, G. Z. Xie, Y. J. Su, H. F. Du, Z. B. Ye and Y. D. Jiang, *Nanotechnology*, 2016, **27**, 065502.

108 M. Ikram, H. Lv, Z. Liu, M. Khan, L. J. Liu, F. Raziq, X. Bai, M. Ullah, Y. Zhang and K. Y. Shi, *Chem. Mater.*, 2020, **32**, 7215–7225.

109 X. Xin, Y. Zhang, X. Guan, J. Cao, W. Li, X. Long and X. Tan, *ACS Appl. Mater. Interfaces*, 2019, **11**, 9438–9447.

110 N. Goel, R. Kumar, S. K. Jain, S. Rajamani, B. Roul, G. Gupta, M. Kumar and S. B. Krupanidhi, *Nanotechnology*, 2019, **30**, 314001.

111 J. Jaiswal, A. Sanger, P. Tiwari and R. Chandra, *Sens. Actuators, B*, 2020, **305**, 127437.

112 C. Liu, X. W. Chen, H. Y. Luo, B. L. Li, J. Shi, C. Fan, J. H. Yang, M. Zeng, Z. H. Zhou and N. T. Hu, *Sens. Actuators, B*, 2021, **347**, 130608.

113 J. B. Liu, J. Y. Hu, C. Liu, Y. M. Tan, X. Peng and Y. Zhang, *Rare Met.*, 2020, **40**, 1536–1544.

114 X. Tian, L. J. X. X. Cui, R. J. Zhao, T. Chen, X. C. Xiao and Y. D. Wang, *J. Mater. Chem. A*, 2022, **10**, 5505–5519.

115 Y. Q. Ding, X. Z. Guo, D. L. Kuang, X. F. Hu, Y. Zhou, Y. He and Z. G. Zang, *J. Hazard. Mater.*, 2021, **416**, 126218.

116 Q. Yue, Z. Z. Shao, S. L. Chang and J. B. Li, *Nanoscale Res. Lett.*, 2013, **8**, 425.

117 W. F. Jiang, K. F. Chen, J. W. Wang, D. Geng, N. A. D. Lu and L. Li, *Mater. Res. Express*, 2021, **8**, 055010.

118 Y. T. Han, D. Huang, Y. G. Ma, G. L. He, J. Hu, J. Zhang, N. T. Hu, Y. J. Su, Z. H. Zhou, Y. F. Zhang and Z. Yang, *ACS Appl. Mater. Interfaces*, 2018, **10**, 22640–22649.

119 A. P. Lee and B. J. Reedy, *Sens. Actuators, B*, 1999, **60**, 35–42.

120 N. Barsan and U. Weimar, *J. Electroceram.*, 2001, **7**, 143–167.

121 D. Z. Zhang, Y. E. Sun, C. X. Jiang, Y. Yao, D. Y. Wang and Y. Zhang, *Sens. Actuators, B*, 2017, **253**, 1120–1128.

122 D. Z. Zhang, J. F. Wu, P. Li and Y. H. Cao, *J. Mater. Chem. A*, 2017, **5**, 20666–20677.

123 Y. Fu, J. Z. Li and H. Y. Xu, *Mater. Sci. Semicond. Process.*, 2020, **114**, 105073.

124 Y. S. Shim, K. C. Kwon, J. M. Suh, K. S. Choi, Y. G. Song, W. Sohn, S. Choi, K. Hong, J. M. Jeon and S. P. Hong, *ACS Appl. Mater. Interfaces*, 2018, **10**, 31594–31602.

125 B. L. Liu, L. Chen, G. Liu, A. N. Abbas, M. Fathi and C. W. Zhou, *ACS Nano*, 2014, **8**, 5304–5314.

126 T. T. Xu, Y. Y. Pei, Y. Y. Liu, D. Wu, Z. F. Shi, J. M. Xu, Y. T. Tian and X. J. Li, *J. Alloys Compd.*, 2-17, **725**, 253–259.

127 H. H. Hau, T. T. H. Duong, N. K. Man, T. T. V. Nga, C. T. Xuan, D. T. T. Le, N. V. Toan, C. M. Hung, N. V. Duy, N. V. Hieu and N. D. Hoa, *Sens. Actuators, A*, 2021, **332**, 113137.

128 S. Y. Cho, S. J. Kim, Y. Lee, J.-S. Kim, W. B. Jung, H. W. Yoo, J. Kim and H. Jung, *ACS Nano*, 2015, **9**, 9314.

129 R. Kumar, P. K. Kulriya and M. Kumar, *Nanotechnology*, 2018, **29**, 464001.

130 R. Kumar, N. Goel and M. Kumar, *ACS Sens.*, 2017, **2**, 1744–1752.

131 P. Chen, J. Y. Hu and Y. Zhang, *ACS Appl. Mater. Interfaces*, 2021, **4**, 5981–5991.

132 K. Rathi, A. N. Kumar and K. Pal, *Nanotechnology*, 2020, **31**, 395504.

133 P. Bharathi, S. Harish, G. Mathankumar, M. K. Mohan, J. Archana, S. Kamalakannan, M. Prakash, M. Shimomura and M. Navaneethan, *Appl. Surf. Sci.*, 2022, **600**, 154086.

134 H. E. Bai, H. Guo, C. Feng, J. Wang, B. Liu, Z. L. Xie, F. Q. Guo, D. J. Chen, R. Zhang and Y. D. Zheng, *Sens. Actuators, B*, 2022, **368**, 132131.

135 Z. M. Yang, D. Z. Zhang and H. N. Chen, *Sens. Actuators, B*, 2019, **300**, 127037.

136 M. Ikram, L. Liu, Y. Liu, M. Ullah, L. Ma and S. U. H. Bakhtiar, *Nanoscale*, 2019, **11**, 8554–8564.

137 L. J. Liu, M. Ikram, L. F. Ma, X. Y. Zhang, H. Lv, M. Ullah, M. Khan, H. T. Yu and K. Y. Shi, *J. Hazard. Mater.*, 2020, **393**, 122325.

138 Q. N. Zhao, W. Z. Zhou, M. X. Zhang, Y. Wang, Z. H. Duan, C. L. Tan, B. H. Liu, F. P. Ouyang, Z. Yuan and H. L. Tai, *Adv. Funct. Mater.*, 2022, **32**, 2203528.

139 N. Kanaujiya, A. K. Golimar, P. C. Pandey and J. G. D. Varma, *AIP Conf. Proc.*, 2018, **1953**, 030142, DOI: 10.1063/1.5032477.

140 A. Taufik, Y. Asakura, T. Hasegawa and S. Yin, *ACS Appl. Nano Mater.*, 2021, **4**, 6861–6871.

141 S. Ramu, T. Chandrakalavathi, G. Murali, K. S. Kumar, A. Sudharani, M. Ramanadha, K. R. Peta, R. Jeyalakshmi and R. P. Vijayalakshmi, *Mater. Res. Express*, 2019, **6**, 085075.

142 S. Y. Hou, R. Pang, S. L. Chang, L. Ye, J. Xu, X. C. Wang, Y. J. Zhang, Y. Y. Shang and A. Y. Cao, *ACS Appl. Mater. Interfaces*, 2020, **12**, 29778–29786.

143 D. Wu, Z. H. Lou, Y. G. Wang, T. T. Xu, Z. F. Shi, J. M. Xu, Y. T. Tian and X. J. Li, *Nanotechnology*, 2017, **28**, 435503.

144 X. X. He, Z. H. Ying, F. Wen, L. L. Li, X. L. Zheng, P. Zheng and G. F. Wang, *Mater. Sci. Semicond. Process.*, 2021, **134**, 105997.

145 Y. P. Miao, H. W. Bao, W. Fan, Y. Li and F. Ma, *Surf. Interfaces*, 2021, **27**, 101580.

146 B. Zhao, C. Y. Li, L. L. Liu, B. Zhou, Q. K. Zhang, Z. Q. Chen and Z. Tang, *Appl. Surf. Sci.*, 2016, **382**, 280–287.

147 S. Sharma, A. Kumar and D. Kaur, *AIP Conf. Proc.*, 2018, **1953**, 030261.

148 S. Singh and S. Sharma, *AIP Conf. Proc.*, 2021, **2265**, 030690.

149 D. Z. Zhang, C. X. Jiang and Y. E. Sun, *J. Alloys Compd.*, 2017, **698**, 476–483.

150 S. Singh, S. Sharma, R. C. Singh and S. Sharma, *Appl. Surf. Sci.*, 2020, **532**, 147373.

151 S. Singh, R. M. Sattigeri, S. Kumar, P. K. Jha and S. Sharma, *ACS Omega*, 2021, **6**, 11602–11613.

152 A. Liu, S. Y. Lv, L. Jiang, F. M. Liu, L. J. Zhao, J. Wang, X. L. Hu, Z. J. Yang, J. M. He, C. G. Wang and G. Y. Lu, *Sens. Actuators, B*, 2021, **332**, 129444.

153 A. Q. Jian, J. H. Wang, H. Y. Lin, S. Q. Xu, D. Han, Z. Y. Yuan and K. Zhuo, *ACS Omega*, 2022, **7**, 11664–11670.

154 S. Singh, J. Deb, U. Sarkar and S. Sharma, *ACS Sustainable Chem. Eng.*, 2021, **9**, 7328–7340.

155 D. Z. Zhang, Z. L. Wu, P. Li, X. Q. Zong, G. K. Dong and Y. Zhang, *Sens. Actuators, B*, 2018, **258**, 895–905.

156 K. J. Yoon, S. I. Lee, H. An, J. Kim, J. W. Son, J. H. Lee, H. J. Je, H. W. Lee and B. K. Kim, *Int. J. Hydrogen Energy*, 2014, **39**, 3868–3878.

157 S. E. Hosseini and M. A. Wahid, *Renewable Sustainable Energy Rev.*, 2016, **57**, 850–866.

158 M. M. Y. A. Alsaif, S. Balendhran, M. R. Field, K. Latham, W. Wlodarski, J. Z. Ou and K. K. Zadeh, *Sens. Actuators, B*, 2014, **192**, 196–204.

159 F. K. Perkins, A. L. Friedman, E. Cobas, P. M. Campbell, G. G. Jernigan and B. T. Jonker, *Nano Lett.*, 2013, **13**, 668–673.

160 M. V. Bollinger, J. V. Lauritsen, K. W. Jacobsen, J. K. Nørskov, S. Helveg and F. Besenbacher, *Phys. Rev. Lett.*, 2001, **87**, 196803.

161 K. Dolui, I. Rungger and S. Sanvito, *Phys. Rev. B: Condens. Matter Mater. Phys.*, 2013, **87**, 165402.

162 A. Castellanos-Gomez, N. Agrait and G. Rubio-Bollinger, *Appl. Phys. Lett.*, 2010, **96**, 213116.

163 Z. Zhang, K. Chen, Q. Zhao, M. Huang and X. P. Ouyang, *Mater. Res. Express*, 2020, **7**, 015501.

164 D. H. Baek and J. Kim, *Sens. Actuators, B*, 2017, **250**, 686–691.

165 H. D. Mai, S. Jeong, T. K. Nguyen, J. S. Youn, S. Ahn, C. M. Park and K. J. Jeon, *ACS Appl. Mater. Interfaces*, 2012, **13**, 14657–14665.

166 S. L. Yang, G. Lei, Z. G. Lan, W. Xie, B. P. Yang, H. X. Xu, Z. Wang and H. S. Gu, *Int. J. Hydrogen Energy*, 2019, **44**, 7725–7733.

167 W. Wu, Z. Liu, L. A. Jauregui, Q. Yu, R. Pillai, H. Cao, J. Bao, Y. P. Chen and S. S. Pei, *Sens. Actuators, B*, 2010, **150**, 296–300.

168 C. Pijolat, G. Tournier, P. Breuil, D. Matarin and P. Nivet, *Sens. Actuators, B*, 2002, **82**, 166–175.

169 C. M. Wu, K. G. Motora, G. Y. Chen, D. H. Kuo and N. S. Gultom, *Front. Mater. Sci.*, 2022, **9**, 831725.

170 A. Saravanan, B. R. Huang, J. P. Chu, A. Prasannan and H. C. Tsai, *Sens. Actuators, B*, 2019, **292**, 70–79.

171 D. Kathiravan, B. R. Huang, A. Saravanan, A. Prasannan and P. D. Hong, *Sens. Actuators, B*, 2019, **279**, 138–147.

172 (*a*) A. Venkatesan, S. Rathi, I. Y. Lee, J. Park, D. Lim, M. Kang, H. I. Joh, G. H. Kim and E. S. Kannan, *Nanotechnology*, 2017, **28**, 365501.

173 D. Z. Zhang, Y. E. Sun, C. X. Jiang and Y. Zhang, *Sens. Actuators, B*, 2017, **242**, 15–24.

174 L. Z. Hao, Y. J. Liu, W. Gao, Y. M. Liu, Z. D. Han, L. Q. Yu, Q. Z. Xue and J. Zhu, *J. Alloys Compd.*, 2016, **682**, 29–34.

175 A. V. Agrawal, R. Kumar, S. Venkatesan, A. Zakhidov, Z. Zhu, J. M. Bao and M. Kumar, *Appl. Phys. Lett.*, 2017, **111**, 093102.

176 S. L. Yang, Z. Chen, Z. Wang, G. Lei, J. Xiong, H. X. Xu and H. S. Gu, *Sens. Actuators, B*, 2022, **367**, 132026.

177 V. Munusami, K. Arutselvan, S. Vadivel and S. Govindasamy, *Ceram. Int.*, 2022, **48**, 29322–29331.

178 A. K. Vivekanandan, B. R. Huang, D. Kathiravan, A. Saravanan, A. Prasannan, H. C. Tsai and S. H. Chen, *J. Alloys Compd.*, 2021, **854**, 157102.

179 J. F. Wu, D. Z. Zhang and Y. H. Cao, *J. Colloid Interface Sci.*, 2018, **529**, 556–567.

180 B. Chakraborty, I. Maity, P. Chung, M. Ho and P. Bhattacharyya, *IEEE Sens. J.*, 2021, **21**, 16484–16491.

181 X. X. Deng, X. Y. Liang, S. P. Ng and C. M. L. Wu, *Appl. Surf. Sci.*, 2019, **484**, 1244–1252.

182 D. Z. Zhang, C. X. Jiang and X. Y. Zhou, *Talanta*, 2018, **182**, 324–332.

183 D. Z. Zhang, X. Fan, A. J. Yang and X. Q. Zong, *J. Colloid Interface Sci.*, 2018, **523**, 217–225.

184 X. Li, J. Wang, D. Xie, J. L. Xu, Y. Xia, L. Xiang and S. Komarneni, *Mater. Lett.*, 2017, **189**, 42–45.

185 D. Z. Zhang, C. X. Jiang and J. F. Wu, *Sens. Actuators, B*, 2018, **273**, 176–184.

186 X. Li, J. Wang, D. Xie, J. L. Xu, Y. Xia, W. W. Li, L. Xiang, Z. M. Li, S. W. Xu and S. Komarneni, *Nanotechnology*, 2017, **28**, 325501.